The Brazilian Earth System Model version 2.5: Evaluation of its CMIP5 historical simulation

Sandro F. Veiga[1], Paulo Nobre[2], Emanuel Giarolla[3], Vinicius Capistrano[4], Manoel Baptista Jr.[2], André L. Marquez[2], Silvio Nilo Figueroa[2], José Paulo Bonatti[2], Paulo Kubota[2], Carlos A. Nobre[5]

[1]Earth System Science Center-CCST, National Institute for Space Research (INPE), São José dos Campos 12227-010, São Paulo, Brazil

[2]Center for Weather Forecasting and Climate Studies-CPTEC, National Institute for Space Research (INPE), Cachoeira Paulista 12630-000, São Paulo, Brazil

[3]Center for Weather Forecasting and Climate Studies-CPTEC, National Institute for Space Research (INPE), São José dos Campos 12227-010, São Paulo, Brazil

[4]Amazonas State University (UEA), Manaus 69005-010, Amazonas, Brazil

[5]CN Research, São José dos Campos 12544-590, São Paulo, Brazil

Correspondence to: Sandro F. Veiga (sandro.veiga@inpe.br)

Abstract

The performance of the coupled ocean-atmosphere component of the Brazilian Earth System Model version 2.5 (BESM-OA2.5) simulating the historical period 1850-2005 is evaluated. Following climate model validation procedure, in which the atmospheric and oceanic main variabilities are evaluated against observation and Reanalysis datasets, the evaluation particularly focuses the mean climate state and the most important large-scale climate variability patterns simulated in the historical run, which is forced by observed greenhouse gas concentration. The most significant upgrades in the model's components are also presented briefly. BESM-OA2.5 is able to reproduce the most important large-scale variabilities, particularly over the Atlantic (e.g. the North Atlantic Oscillation, the Atlantic Meridional Mode and the Atlantic Meridional Overturning Circulation) and the extratropical modes that occur in both hemispheres. The model's ability in simulating large-scale variabilities indicates its usefulness for seasonal climate prediction and climate change studies.

1. Introduction

Climate Models and their recent extension to become Earth System Models, by the inclusion of biogeochemical cycles, are key tools to investigate climate phenomena which greatly influence human societies (e.g. von Storch, 2010; Flato, 2011). Since 2008 the Brazilian climate community has been engaged in setting up the Brazilian Earth System Model (BESM; Nobre et al., 2013; Giarolla et al., 2015); a major scientific task which has been carried out by Brazilian scientific institutions invoking the critical need to address reliable future climate projections and their potential impacts, particularly over South America. The primary objective encompassed in this effort is to build up the scientific expertise capable to develop and maintain a state-of-the-art Earth System Model. Such an achievement would represent a significant step forward in establishing a scientific tool which can be used in different arrays of research activities. The importance of such undertaking lies in the understanding of the physics of the Earth system to produce and confer credibility to studies of impacts of climate change in different areas of great importance; such as food and water security, tropical ecosystems, natural disasters, and so on. One of the primordial aims of the BESM project is to participate in the Coupled Model Intercomparison Project's sixth phase (CMIP6; Meehl et al., 2014).

The Brazilian Earth System Model (BESM) has been set up at the Brazilian National Institute for Space Research (INPE). At present, it consists of a land-ocean-atmosphere coupled model, in which the coupling is done through the Flexible Modeling System (FMS) coupler, developed at the Geophysical Fluid Dynamics Laboratory (GFDL) of the National Oceanic and Atmospheric Administration (NOAA).

The inclusion of aerosols (as read-in fields) and atmospheric chemistry components are in the phase of implementation and tests. Currently, work has been done on activate the biogeochemical model (TOPAZ) within the MOM5 in order to simulate biogeochemical cycles in future simulations.

The previous version of BESM (BESM-OA2.3) was firstly evaluated in Nobre et al. (2013). This version showed a significant bias on precipitation in the tropical region, with a deficient representation of precipitation in the Amazon region. In order to improve these aspects, studies were conducted to ameliorate cloud parameterizations over the tropics, which improved the precipitation over the same region and the representation of Convergence Zones over both the Atlantic and Pacific Oceans basins (Bottino and Nobre, 2018). Main changes of the current version relate to BESM's atmospheric model, with modifications in the surface wind field and its parameterizations, described in Capistrano et al. (2018). The updated version presented in this manuscript is BESM-OA2.5.

From the operational point of view, BESM-OA2.3 is already being used for extended weather forecast (10-30 days) to seasonal climate prediction (three months), as well as for producing global climate change scenarios (Nobre et al., 2013) and to provide atmospheric and oceanic boundary conditions to regional climate models for dynamical downscaling of climate change scenarios (Chou et al., 2014).

This overview paper describes the most important developments and improvements in the model components, presenting the simulation of recent past mean climate conditions and major large-scale climate phenomena. In section 2 the BESM-OA2.5 components and experimental design are briefly described; section 3 presents the

methodology and the observed data used to evaluate the model; section 4 presents the evaluation of the historical simulation, in which are evaluated the most important atmospheric and oceanic variables regarding to their climatological fields and the prominent large-scale phenomena of the climate system; finally, section 5 presents the summary.

2 Model Description and Simulation Experiment Design

2.1 BESM-OA2.5

The atmospheric component of BESM-OA2.5 is the Brazilian Global Atmospheric Model (BAM; Figueroa et al., 2016) developed at Center for Weather Forecasting and Climate Studies (CPTEC/INPE). It is a primitive equation model with spectral representation with triangular truncation at the wave number 62, corresponding to a grid resolution of approximately $1.875° \times 1.875°$, and 28 sigma levels in the vertical, with uneven increment between the levels, i.e. T62L28 resolution. As mentioned before, it is in the atmospheric component which resides the main differences between BESM-OA2.5 and BESM-OA2.3 (Nobre et al., 2013). The new version shows a key improvement in the energy balance at the top of the atmosphere, by reducing the mean global bias from -20 W m^{-2} in version BESM-OA2.3 to -4 W m^{-2} in the current version (Capistrano et al. 2018). Version 2.5 of BESM incorporates the formulation presented in Jiménez et al. (2012) for the representation of the wind, humidity and temperature in the surface layer. The model runs without flux correction or adjustment. The physics parameterizations for the continental processes are based on the Simplified Simple Biosphere Model (SSiB) land surface model (Xue et al., 1991), in

shortwave radiation Clirad scheme (Tarasova et al. 2007; Chou and Suarez 1999), in

longwave radiation Harshvardhan scheme (Harshvardhan et al., 1987), in Cloud

microphysics Ferrier scheme (Ferrier et al. 2002), in the turbulence level 2 module

(Mellor and Yamada, 1982), in the gravity wave module (Anthes, 1977), in the deep

convection module (Arakawa and Schubert, 1974; Grell and Dévényi, 2002), and in the

shallow convection module (Tiedtke, 1983). More details can be found in Figueroa et

al. (2016) and in Capistrano et al. (2018).

The oceanic component of BESM-OA2.5 is the Modular Ocean Model version

4p1 (MOM4p1; Griffies, 2009) developed at GFDL, which includes the Sea Ice

Simulator (SIS) built-in ice model (Winton, 2000). There are no changes in the physics

parameterizations from those used in BESM-OA2.3. The horizontal grid resolution in

the zonal direction is $1\,^{\circ}$ and in the meridional direction it varies uniformly from $1/4\,^{\circ}$

between $10\,^{\circ}$S and $10\,^{\circ}$N to $1\,^{\circ}$of resolution at $45\,^{\circ}$and to $2\,^{\circ}$of resolution at $90\,^{\circ}$, in both

hemispheres. The vertical resolution has 50 levels with approximately 10 m resolution

in the upper 220 m, increasing gradually to about 370 m resolution at deeper levels. The

oceanic model spin-up was done in a manner similar to that of Nobre et al. (2013) and

Giarolla et al. (2015), in which is begin the spin-up run from rest, and the T-S structure

of the oceans of Levitus (1982). The initial stage of the ocean model spin-up was done

over a 13 years period, forced by climatological atmospheric fields (winds, solar

radiation, air temperature and humidity, and precipitation). It was then integrated by an

additional 58 years period, forced by interannually varying atmospheric fields from

Large and Yeager (2009), while the river discharges and the sea ice variables were kept

at their respective monthly mean climatological values. The forced ocean model run

was used to save the oceanic dynamical and thermodynamical structures in order to be used in the initialization of future coupled model experiments.

The atmospheric and oceanic models are coupled via the Flexible Modeling System (FMS) coupler, which was also developed at GFDL and incorporated in MOM4p1. The atmospheric model receives SST and ocean albedo from the ocean and sea ice models at hourly time steps. On the other hand, the oceanic model receives information about freshwater (liquid and solid precipitation), momentum fluxes (winds at 10 m), specific humidity, heat, vertical diffusion of velocity components and surface pressure, all also at hourly time steps. Wind stress fields are computed within MOM4p1 using Monin-Obukhov scheme (Obukhov, 1971). In coupled simulations, the ocean temperature and salinity restoration options are turned off.

2.2 Experiments design

A set of numerical experiments were carried out with the coupled ocean-atmosphere version of BESM-OA2.5, following the CMIP5 experiment design protocol (Taylor et al., 2012), and shown schematically in Figure 1. Out of those experiments listed below, only the Historical simulation is evaluated in this paper:

- Historical: the simulation runs over the period 1850−2005 (156 years), forced by atmospheric equivalent CO_2 observed historical concentration (greenhouse gas only) over this period, based on CMIP5 protocol.
- piControl: it runs for 1140 years, forced by invariant pre-industrial atmospheric CO_2 concentration level (280 ppmv).
- Abrupt 4×CO2: it runs for 1000 years, consisting of an abrupt quadruplication of

1   the atmospheric CO_2 concentration level from the piControl simulation.

2 ● RCP4.5: it runs over the period 2006−2105 (100 years), forced by the time series

3   of greenhouse gases level projected by the Representative Concentration

4   Pathways 4.5 (RCP4.5), based on CMIP5 protocol. This simulation continues

5   the historical simulation throughout the 21th century, reaching the radiative

6   atmospheric forcing of 4.5 W m^{-2} in 2100.

7 ● RCP8.5: same as the RCP4.5 simulation, but forced by the time series of

8   greenhouse gases level projected by the Representative Concentration Pathways

9   8.5 (RCP8.5), based on CMIP5 protocol; i.e., reaching the radiative atmospheric

10   forcing of 8.5 W m^{-2} in 2100.

11 The ocean stand-alone runs for 71 years (13 years period of ocean model spin-up forced by

12 climatological atmospheric fields plus 58 years period forced by interannually varying

13 atmospheric fields). Then a spin-up of the fully coupled model is done for 100 years. The ocean

14 and atmosphere states at the end of this 100 years long integration are used as the initial

15 condition for the piControl simulation. The model's versions are slightly different for 100 years

16 spin-up and the piControl run, in the parameterizations of the land ice albedo and cloud

17 microphysics. The Historical simulation uses as initial conditions information of the 14th year

18 provided by the piControl simulation. The piControl simulation shows stable conditions after a

19 fast adjustment over the first 13 years of simulation (figure not shown). Therefore, it is assumed

20 that the Historical simulation has a spin-up of 113 years. The analysis of the piControl and

21 4×CO2 simulations are described in Capistrano el al. (2018) and Nobre et al. (2018, in

22 preparation). Capistrano et al. (2018) estimates that BESM-OA2.5 has an equilibrium

23 climate sensitivity of 2.96 ℃ for the abrupt 4×CO2 experiment. This value is within the

24 range from 2.07 to 4.74 ℃ that has been computed for 25 CMIP5 models and close to

25 the ensemble averaged value (3.30 ℃).

3. Methods and Data

To evaluate the outputs of the BESM-OA2.5 historical simulation, comparisons are done against observed datasets and Reanalysis products. The atmospheric fields are from the Twentieth-Century Reanalysis dataset version 2 (20CRv2; Compo et al., 2011) with a global horizontal resolution of $2° \times 2°$ and 24 vertical levels (https://www.esrl.noaa.gov/psd/data/gridded/data.20thC_ReanV2.html); the precipitation dataset is obtained from Global Precipitation Climatology Project version 2.2 Combined Precipitation Dataset (GPCP; Adler et al., 2003; Huffman et al., 2009) with global horizontal resolution of $2.5° \times 2.5°$ (http://rda.ucar.edu/datasets/ds728.2/#!description) and from the CPC Merged Analysis of Precipitation (CMAP; Xie and Arkin, 1997) with global horizontal resolution of $2.5° \times 2.5°$ (https://www.esrl.noaa.gov/psd/data/gridded/data.cmap.html); for comparison of the global average air surface temperature, it is used the Hadley Centre-Climate Research Unit Temperature Anomalies version 4 (HadCRUT4, Morice et al., 2012), globally averaged air temperature anomaly at 2 meters time series (https://crudata.uea.ac.uk/cru/data/temperature/); the cloud cover is compared to data from The International Satellite Cloud Climatology Project (ISCCP D2; Rossow and Schiffer, 1999) with global horizontal resolution of $2.5° \times 2.5°$ (https://isccp.giss.nasa.gov/products/onlineData.html); finally, for Sea Surface Temperature (SST) comparisons it is used the Extended Reconstructed Sea Surface Temperature version 4 (ERSSTv4, Huang et al., 2015) available on a $2° \times 2°$ grids resolution (https://www.esrl.noaa.gov/psd/data/gridded/data.noaa.ersst.v4.html).

To identify the main modes of climate variability, all analyses presented in the

paper are done using detrended data sets anomalies. Detrended data sets are obtained by removing the linear trend based on a least squares regression. Analysis using monthly data sets, the annual cycle was removed by subtracting climatological monthly means from the respective individual month. Prior to performing the analysis, the model's data sets were interpolated to the grid resolution of the respective observation or Reanalysis data sets used for comparison.

The Empirical Orthogonal Function analysis (EOF; Hannachi et al., 2007) is used to analyze the capacity of the model in simulating major modes of climate variability and compare them with observations. Prior to performing the EOF calculations, the data were weighted by the square root of the cosine of latitude. The results of the EOF maps are shown as the original data anomalies regressed onto the normalized Principal Component (PC) time series, i.e. by the standard deviation.

In this paper, in order to evaluate the periodicity of the phenomena, it is applied the power spectrum technique based on Fourier Analysis on the normalized time series, in which the normalization is done by their long-term monthly standard deviation.

To have a better insight of BESM-OA2.5 performance of the global average near-surface air temperature and on the average SST along both equatorial Pacific and Atlantic, a comparison with 11 CMIP5 models is carried out. Since BESM-OA2.5 historical simulation is forced only by observed CO_2 equivalent concentration, for the comparison it is chosen the historical simulation forced only by greenhouse gas (historical GHG) shown in Table 1.

4. Results

4.24.1 Mean Climate State

In this section, the most important atmospheric and oceanic variables are evaluated regarding their climatological fields, either globally or over regions in which their representation are key elements of the climate system.

4.1.1 Mean Surface Air Temperature

The evolution of global surface air temperature throughout the industrial era is a key element to analyze the long-term model behavior while being forced by the observed conditions. The HadCRUT4 observation and BESM-OA2.5 time series of the globally averaged air temperature anomaly at 2 meters are shown in Figure 2. The time series are annual mean anomalies relative to the period 1850–1879. BESM-OA2.5 simulation of the global average surface air temperature evolution follows closely the observed time series. However, since BESM-OA2.5 does not have the representation of aerosols and consequently its cooling effects, the rate surface air warming should be higher similarly to the remaining models (the grey shadow in Figure 2). In order to compare BESM-OA2.5 with the selected CMIP5 models, the grey shadow represents the spread of the minimum and the maximum values of anomalies at each year among the 11 models (Table 1). In this comparison, it is used the historical GHG simulation, in which the models are only forced by well-mixed greenhouse gases (mainly carbon dioxide, methane, and nitrous oxides), without the cooling resulting from the direct and indirect effects of aerosols, volcanos and effects of the land use change. Thus, the CMIP5 models show a warmer tendency compared with the observations (see Jones et al., 2013 for more details). Although BESM-OA2.5 has the same forcing conditions it does not show the warming tendency of remaining models. With exception of GFDL-

1   ESM2M (1861−2005) and HadGEM2-ES (1860−2005), all the remaining CMIP5

2   models span their simulations throughout the period 1850−2005 and their respective

3   anomalies are from the period 1850−1879. For GFDL-ESM2M and HadGEM2-ES, the

4   anomalies are computed relative to the periods 1861−1890 and 1860−1889,

5   respectively.

6   The net radiation at the top of atmosphere (TOA) has a negative bias and net of

7   the ocean/atmosphere heat flux has a positive bias (Fig. 3). The net radiation at TOA

8   has a mean value of -4.20 W m^{-2} and the net ocean/atmosphere heat flux has a mean

9   value of 1.16 W m^{-2} in the first 50 years. The net radiation imbalance at TOA is related

10   to significant loss of energy at TOA both from the outgoing long-wave radiation and

11   outgoing short-wave radiation. Throughout the simulation the net radiation at TOA

12   becomes less negative due to the increasing CO_2 on the atmosphere and consequential

13   increasing atmospheric heat content. Part of this heat is transferred into the ocean as

14   positive net of the ocean/atmosphere heat flux increasing indicates. The negative net

15   radiation at TOA and the positive ocean/atmosphere heat flux are likely the reason for

16   the weak warming observed in the Historical simulation (Fig. 2), since the atmosphere

17   is losing heat to the outer space and into ocean during the simulation.

18   **4.1.2 Mean Precipitation**

19   One of the key points in evaluating a Climate Model is to gauge its ability to

20   simulate the hydrological cycle due to its importance to the energy balance of the

21   climate system. Figure 4 shows the spatial distribution of annual mean precipitation for

22   (a) BESM-OA2.5, (b) GPCP dataset, and the spatial distribution of annual mean

23   precipitation bias (c) for BESM-OA2.5 relative to the GPCP dataset and (d) for BESM-

OA2.5 relative to the CMAP dataset. The spatial annual mean precipitation are averaged values over the periods 1971–2000 and 1979–2008, for BESM-OA2.5, and GPCP and CMAP datasets, respectively. The global model's mean biases are similar for GPCP (0.3 mm day^{-1}) and CMAP (0.4 mm day^{-1}). In the case of the global model's rmse biases, they are also similar for GPCP (1.4 mm day^{-1}) and CMAP (1.5 mm day^{-1}). BESM-OA2.5 is able to reproduce global observed patterns of precipitation and indicates a slight improvement in the global mean precipitation simulation compared with the previous version (BESM-OA2.3). The spatial average biases are 0.3 mm day^{-1} and 0.5 mm day^{-1}, and the rmse are 1.4 mm day^{-1} and 1.7 mm day^{-1} for BESM-OA2.5 and BESM-OA2.3, respectively. The improvements are particularly seen in the Pacific and Atlantic Ocean areas, where BESM-OA2.5 reduces the positive bias that extends to subtropical southeast Pacific and both north and south Atlantic subtropics observed in BESM-OA2.3 (see Fig. 6a of Nobre et al., 2013). Despite these improvements, BESM-OA2.5 still generates a strong negative bias over the Amazon region. This is a particular concern since an important aim is related to the model for future climate projections in the region. Based on the progress observed from BESM-OA2.3 to BESM-OA2.5, work on cloud parametrizations that can improve the precipitation over the Amazon is still carried out. Nevertheless, some state-of-the-art models show deficiencies in generating precipitation over the Amazon region. This is the case of the IITM-ESM (Fig. 5; Swapna et al., 2018), although the bias is more confined to the north of the Amazon and NESM that has a more distributed bias over the region (Fig. 9; Cao et al., 2018). The Indian subcontinent region also has a significant negative bias and strong positive bias appears over the Indian Ocean and in the South Pacific Convergence Zone (SPCZ). Such strong positive bias over the Indian Ocean (near the African coast) is also

1   identified in different versions of CCSM model (Fig. 5; Gent et al., 2011).

2   In order to draw an associated global atmospheric circulation associated with the

3   deficient precipitation over both the Amazon and Indian regions, it is computed the

4   global anomalies of the velocity potential and the divergence of the wind at 200 hPa

5   pressure level, and shown in Figure 5. The velocity potential and divergent wind

6   anomalies are averaged over the period 1971−2000 for BESM-OA2.5 outputs (Fig. 5a),

7   Reanalysis (Fig. 5b) and the difference BESM-OA2.5 minus Reanalysis (Fig. 5c, 5d and

8   5e). Figure 5c shows anomalous convergence over the Amazonian and Indian regions,

9   resulting of the model's deficient capacity for creating convection and consequently in

10   generating precipitation. Figures 5d and 5e show the velocity potential and wind

11   divergence separated by seasons. For the Amazonian rainfall season, which occurs

12   during MAM, it is possible to observe anomalous convergence at high levels of the

13   atmosphere (Fig 5d). The equivalent result is observed for the Indian region for the JJA

14   season (Fig. 5e).

15   Figure 6 shows zonally averaged precipitation during the four seasons. For this

16   comparison, results of BESM-OA2.3 used in Nobre et al. (2013) are also shown. Both

17   versions are able to reproduce the maximum peaks of precipitation in both tropical and

18   subtropical regions. BESM-OA2.5 shows a negative bias from around 40 ° latitude

19   poleward in both hemispheres. In the seasons DJF, JJA and SON, BESM-OA2.5 has a

20   positive bias on the peak of maximum precipitation corresponding to the ITCZ. In

21   MAM season the model still fails to perform the interhemispheric transition of the

22   ITCZ. However, the JJA season shows that BESM-OA2.5 is able to do the transition

23   completely, whilst BESM-OA2.3 shows a double ITCZ in JJA and SON seasons. The

1 double ITCZ problem is one of the most significant biases that persist in climate models

2 (e.g. Hwang and Frierson, 2013; Li and Xie, 2014; Tian, 2015). With the exception of

3 the MAM season, BESM-OA2.5 shows identical zonal precipitation to the observations,

4 although with a generally positive bias. It should be noted that BESM-OA2.5 has a

5 rapid precipitation decline at high latitudes. The model shows peaks of precipitation at

6 the mid-latitudes related to the storm tracks and less precipitation at the subtropics

7 compared to the GPCP dataset.

8   Figure 7 shows the general characteristics of cloudiness over the globe simulated

9 by the model. In particular, Figure 7a shows that the model underestimates cloudiness in

10 most part of the globe, with significant exceptions of the high latitudes in the boreal

11 hemisphere and in the southern subequatorial regions of the Pacific and Atlantic Oceans

12 when compared to observations. Globally, BESM-OA2.5 has a cloudiness negative bias

13 of -13.9 % with a root-mean-square-error of 19.9 %. The periods used are $1971-2000$

14 and $1984-2009$ for BESM-OA2.5 and ISCCP, respectively. The model fails to generate

15 clouds in the high latitudes of the austral hemisphere, as can be observed in Figure 7b,

16 where the percentage of cloud cover is negligible. The reason for such lack of simulated

17 cloudiness in this region is not clear yet. However, through the Figure 7b it is possible

18 to see the meridional variation of cloud cover simulated by the model is similar to the

19 observation.

20 **4.1.3 Zonal Atmospheric Mean State**

21   Figures 8 and 9 present the analysis of the zonally averaged vertical profiles of

22 air temperature and zonal wind for all seasons simulated by BESM-OA2.5 and the

23 respective bias relative to the 20CRv2 Reanalysis dataset, in which all data are time

averaged over the period 1971−2000. BESM-OA2.5 has a large positive air temperature bias that appears above 250 hPa height (Fig. 8) in subpolar and polar regions in all seasons. This result indicates that the model warms abnormally in the tropopause and the lower stratosphere in polar regions. The warm bias is stronger in DJF and MAM seasons over the northern polar region, reaching a maximum bias of 20 ℃ in the DJF season. Such a bias is a matter of concern since other models, despite present strong bias in the Polar Regions, does not show such a strong bias. BNU-ESM presents positive biases up to 10 ℃ in the austral hemisphere during the season JJA (Fig. 3a; Ji et al., 2014) and NorESM1-M presents negative biases (~ -10 ℃) during the seasons DJF and JJA (Fig. 9; Bentsen et al., 2013). In the lower and middle troposphere, the model shows a negative temperature bias, which is stronger in the lower troposphere over the polar region in the respective winter-spring seasons in both hemispheres, i.e. DJF and MAM over the North Pole, and JJA and SON over the South Pole. This negative bias reaches its maximum of −10 ℃ over the South Pole in SON. This negative bias over the troposphere has already been reported to occur in many CMIP5 models (see Charlton-Perez et al., 2013; Tian et al., 2013).

Concerning to the zonal wind, BESM-OA2.5 simulates a much weaker wind speed at the tropopause and stratosphere over the boreal hemisphere, mainly in the DJF season, which has a maximum negative bias of -26 m s^{-1} at 50−30 hPa (Fig. 9a). This bias is out of the range (-10 m s^{-1} to 10 m s^{-1}) that some models presents, as NorESM1-M (Fig. 10; Bentsen et al., 2013) or NESMv3 (Fig. 10d; Cao et al., 2018). The tropospheric jets and their seasonal migration are reasonably well simulated, although the eastward wind is stronger at subtropics with the maximum positive bias of 12 m s^{-1}

occurring at 300−100 hPa in the MAM season.

4.1.4 Ocean Mean State

The global distribution and the range values of the sea surface temperature (SST) are important characteristics of the mean climate state. Figure 10 shows the spatial map of the annual mean SST for (a) BESM-OA2.5, (b) ERSSTv4 and (c) the bias for BESM-OA2.5 relative to the ERSSTv4 dataset. BESM-OA2.5 has a warm SST bias which spreads throughout all oceans, contrasting with the negative biases which most of the CMIP5 models show over the North Pacific and North Atlantic Oceans (see Wang et al., 2014). However, the extreme values found in the south of Greenland and in the North Pacific, where it reaches ~6 ℃, is well within the range of biases reported by other models, as NorESM1-M (Fig. 12b; Bentsen et al., 2013) or IITM-ESM (Fig. 3; Swapna et al., 2018). Such warm bias does not appear in the tropical and subtropical regions in the BESM-OA2.3 simulation (Fig. 5a of Nobre et al., 2013), where there are cold SST biases. The spatial average biases are 1.5 ℃ and 0.9 ℃, and the rmse are 1.9 ℃ and 2.1 ℃ for BESM-OA2.5 and BESM-OA2.3, respectively. A notable feature of BESM-OA2.5 is its strong warm SST bias in the North Pacific and in the Californian coast, and south of Greenland. The model still overestimates SSTs in the major eastern coastal upwelling regions. Such a feature is a systematic error observed in different state-of-the-art models, in which the causes can be related to a simulation of a weaker than observed alongshore winds which leads to an underrepresentation of upwelling and alongshore currents (e.g. Humboldt, California and Benguela Currents), and/or the under predicted effects of shortwave radiation due to deficient simulation of stratocumulus clouds over cold waters (see Richter, 2015). Nevertheless, the bias is

1 negligible over the north equatorial Pacific and in large parts of tropical western

2 Atlantic.

3 Figure 11a shows the mean SST along equatorial Pacific for BESM-OA2.5 and

4 ERSSTv4, averaged over the period 1971−2000. The equatorial region is defined over

5 the region between the latitudes 2 °S and 2 °N. The model simulates a warmer mean

6 SST over the western and extreme eastern parts of the equatorial Pacific Ocean. This

7 positive bias is most notable in the western part, where it is about 1.5−2 ℃ warmer than

8 observations and is warmer than the CMIP5 models (shown by the shaded grey area in

9 Figure 11a). But for the extreme eastern part of the basin, the model has a lower bias

10 compared with the CMIP5 models. For most of the central Pacific Ocean, the model has

11 a very good representation of the SST, with a RMSE of 0.14 ℃ between 160 °E and

12 120 °W. The annual cycle of the equatorial Pacific SST anomalies for BESM-OA2.5

13 and ERSSTv4 are shown in figure 11b and c, respectively. BESM-OA2.5 simulates

14 reasonably well the marked annual cycle which occurs on the eastern Pacific, although

15 the negative SST anomalies between July and December are up to 1 ℃ colder than

16 observations. The propagation of the SST anomaly patterns from the eastern to the

17 western part of the Pacific Ocean that occurs throughout the year is not well captured by

18 the model. BESM-OA2.5 shows an annual cycle in the western part of the Pacific

19 Ocean, where observations show a semiannual pattern of SST anomalies. The same

20 methodology is used for the tropical Atlantic. Figure 12a shows that in the Atlantic

21 basin there is a significant bias of ~3 ℃ in the eastern part of the basin. This bias starts

22 in the central Atlantic and it is higher than the CMIP5 models (shown by the shaded

23 grey area in Figure 12a). However, it should be noted that the CMIP5 models also have

24 a warm bias in the eastern part of the tropical Atlantic, which is a problem discussed in

1 previous studies (e.g. Richter et al., 2014 and references therein). Although this warm

2 bias, the tropical Atlantic seasonal SST variation is well simulated by BESM-OA2.5 in

3 particular on the eastern side of the basin, as it can be seen in Figures 12b and c.

4   To evaluate how the global ocean profile evolves throughout the simulation, it is

5 computed the depth-time Hovmöller diagrams of global mean ocean salinity and

6 temperature departures from their respective initial conditions (Fig. 13a and 13b) for

7 Historical simulation. Here initial conditional means the value of the first year of

8 simulation, in this case, the year 1850. The ocean salinity slightly increases below 1000

9 m depth and from 1935 the increase reaches 0.04 PSU between 1500 and 3000 m depth

10 compared with the initial values (Fig. 13a). Above 1000 m depth there is a significant

11 freshening of the ocean waters, with the surface waters salinity decreasing up to 0.18

12 PSU at the end of the simulation. Concerning ocean temperature, a prominent warming

13 occurs from the surface up to 400 m depth (Fig. 13b). This warming is more significant

14 at the end of the simulation (~0.6 °C comparing with initial conditions) and is mostly

15 caused by the ocean warming drift of the model. Fig. 13c shows the same diagram for

16 piControl simulation (during the period in which both simulations are performed in

17 parallel), which also presents the ocean drift. However, the ocean temperature

18 anomalies above 600 m reaches ~0.6 °C in the Historical simulation whereas in the

19 piControl it reaches ~0.4 °C. This difference of 0.2 °C between the two simulations is

20 likely due to the global warming of the planet and consequential increasing heat flux

21 from the atmosphere into the ocean (Fig. 13d). In deeper waters, from 1500 m up to the

22 ocean floor, there is a weaker warming, indicating that the ocean is gaining heat mainly

23 in the upper layers (Fig. 13b). Between 500-1500 m depth, it is observed a cooling

1   tendency respective to initial conditions. Such tendency can mean that the ocean is still

2   drifting from its initial conditions in the Historical simulation.

3   The meridional overturning circulation (MOC) plays an important role in

4   transporting heat from the tropics to higher latitudes of both hemispheres. This is

5   particularly important in the North Atlantic, where the Atlantic Meridional Overturning

6   Circulation (AMOC) has a profound impact on the climate of the surrounding

7   continents (see Buckley and Marshall, 2015). The AMOC in the BESM-OA2.5 historical

8   experiment has the typical structure described in Lumpkin and Speer (2007), with the upper

9   layer of the upper cell, which is the northward flux, depicted in the appropriated depth, from the

10   surface up to ~1000 m (Fig. 14a). However, the upper cell simulated by BESM-OA2.5 is too

11   shallow compared with the RAPID measurements (McCarthy et al., 2015). The depth of the

12   upper cell is 2500 m in the model whereas the measurements show its depth at ~4500 m. This

13   shallow upper cell of the AMOC is a common feature of state-of-the-art climate models (see

14   Menary et al., 2018). The model simulates the northward Antarctic Bottom Water in the ocean

15   floor. The annual mean maximum AMOC strength simulated by BESM-OA2.5 is about

16   15 Sv (1 Sv $\equiv 10^6$ m^3 s^{-1}) between 25 °N and 30 °N at about 850 m depth (see Figure

17   14a). This maximum value is within the 17.2 $\pm$ 4.6 Sv mean strength (with a 10 day

18   filtered root mean square variability of 4.6 Sv) observed by the project RAPID at 26.5 °

19   N (McCarthy et al., 2015). It is also in the range of maximum volume transport strength

20   simulated by the state-of-the-art models of the CMIP5 (Weaver et al., 2012; Cheng et

21   al., 2013). Figure 14b shows the maximum annual mean AMOC strength time series for

22   the historical period at the 30 ° N. For comparison, Figure 14c plots the AMOC

23   maximum volume transport strength measured by the Rapid project over the period

24   April/2004 to October/2015 (http://www.rapid.ac.uk/rapidmoc/rapid_data/datadl.php).

1   Averaging the maximum AMOC strength over the first and the last 30 years of

2   the time series, i.e. over the periods 1850−1879 and 1976−2005 respectively, the result

3   shows a decrease of 11.2 %, from 16.9 Sv to 15.1 Sv in each period, respectively.

4   Modeling results indicate that the AMOC has a multidecadal cycle, however the power

5   spectrum of its strength time series do not show a multidecadal oscillation (not shown).

6   The standard deviation of the detrended maximum AMOC strength time series is 1.4

7   Sv.

8   Figure 15 shows the mean sea ice concentration simulated by BESM-OA2.5 for

9   the end of the winter and the summer seasons for each hemisphere, over the period

10   1971-2000. The thick black lines represent the 15 % climatological values for the period

11   1971-2000 given by the 20CRv2 Reanalysis. The sea ice concentration in the Arctic

12   winter is overestimated in the Atlantic, specifically north of the Scandinavia (Fig. 15a).

13   However, in summer the Arctic sea ice is underestimated (Fig. 15b). In the Antarctica

14   summer the model shows a significant underestimation of the sea ice concentration (Fig.

15   15c). During the Antarctica winter the model generally overestimates the extension of

16   the sea ice concentration over all Southern Ocean (Fig. 15d). Such seasonal sea ice

17   concentration amplitude is likely related to bias radiative net over higher latitudes that

18   the model suffers, which during the winter in each hemisphere tend to generate higher

19   extension of sea ice and during the summer in each hemispheres tend to enhance the sea

20   ice melting compared with the Reanalysis.

22   **4.2 Climate Variability**

23   In this section, we evaluate the most prominent global climate variability

patterns. This allows us to infer the ability of the model in simulating atmospheric internal and ocean-atmosphere coupled variabilities in the climate system correctly.

4.2.1 Tropical Variability

4.2.1.1 El Niño-Southern Oscillation

The El Niño-Southern Oscillation (ENSO) in the equatorial Pacific Ocean is one of the most prominent climate variability phenomena at interannual time scales (Dijkstra, 2006), with strong impacts on regions surrounding the Indian and Pacific Oceans and regions that are influenced by its teleconnections (see McPhaden et al., 2006 and references therein). There are many methods to evaluate the ENSO variability. In the present study, it is applied the EOF to detrended monthly SST anomalies over the tropical Pacific Ocean (30º S−30º N; 240º−70º W) for the period 1950−2005 for both BESM-OA2.5 simulations and ERSSTv4 data. Figures 15a and b show the leading EOF patterns associated with the El Niño/La Niña variability. The model simulates the El Niño/La Niña variability deficiently, with lower amplitude of SST variability and the center of maxima variability confined to the eastward part of the basin. The model's leading EOF explains 17.9 % of the total variance, substantially less than the 45 % explained by observations. The lower amplitude of the simulated El Niño/La Niña can be verified in the power spectrum of the leading Principal Component (PC) shown in Figure 16. Even though the simulation shows two significant peaks between 2−4 years cycle (Fig. 16c), which is within the range of the period cycle given by the leading PC of observations (3−7 years cycle; figure 16d), the amplitude of the simulated variance is lower than that of observations.

1   Figure 17 shows the spatial correlation between detrended monthly anomalies of

2   the Niño-3 index (defined inside the black rectangle area, bounded by 5° S−5° N,

3   90°−150° W) and detrended monthly anomalies of global SST computed for BESM-

4   OA2.5 and ERSSTv4 over the period 1900−2005. The model has not a strong

5   correlation at grid points inside the Niño-3 area, which is a signal that the El Niño/La

6   Niña spatial pattern is weakly simulated. The horseshoe pattern of negative correlation

7   observed in the Pacific Ocean is also weakly simulated by the model, particularly in the

8   westward equatorial part. The positive correlation of observed SST over the Indian

9   Ocean and Niño-3 index is absent in the model's simulation. It is worth mentioning that

10   the model simulates the observed correlation pattern of SST anomalies over the Atlantic

11   Ocean with Ninõ-3 index, although it is not so robust (Figure 17).

12   **4.2.1.2 Atlantic Meridional Mode**

13   The leading modes of coupled ocean-atmosphere variability over the Tropical

14   Atlantic Ocean are the zonal mode, also referred as equatorial mode (Zebiak, 1993; Lutz

15   et al., 2015), and the meridional mode, also referred as the interhemispheric mode

16   (Nobre and Shukla, 1996). The first is an ENSO-like phenomenon that emerges in the

17   Gulf of Guinea mainly in the boreal summer and has a strong impact on West African

18   precipitation (Zebiak, 1993; Lutz et al., 2015). The second is characterized by a cross-

19   equatorial SST gradient associated with a meridional wind stress toward the warmer

20   SST anomalies. The maxima amplitude of the meridional mode occurs during the boreal

21   spring, influencing the precipitation in Northeast Brazil and West Africa (Nobre and

22   Shukla, 1996; Chang et al., 1997; Chiang and Vimont, 2004). The Atlantic Meridional

23   Mode (AMM) has an interannual and decadal temporal scale of variability and is a

result of a thermodynamic coupling between the wind speed, the sea surface evaporation induced by the wind stress, and the SST, mechanism known as Wind-Evaporation-SST feedback (WES feedback, Xie and Philander, 1994; Chang et al., 1997; Xie, 1999). To evaluate the AMM simulations, a joint EOF of SST and wind stress (Taux and Tauy) fields analysis is computed, as such a variability is the response of a coupled ocean-atmospheric system. Figure 18 shows the AMM simulated by BESM-OA2.5, and obtained by observed data. The AMM pattern simulated by the model is similar to obtained from observations, regardless of the weaker gradient pole at the South Atlantic. Nevertheless, the explained variance by the model is very close to the observed one, being respectively, 10.7 % and 11.8 %. The patterns shown in Figure 18 are defined as a positive phase of the AMM, with the inter-hemisphere cross-equatorial wind from south to north, and with corresponding negative SST anomalies over the southern pole and positive SST anomalies over the northern pole (the negative phase of AMM is the reverse pattern). Over the second half of the 20th century, the AMM shows a predominant decadal periodicity of 11−13 years. Figures 18c and d show the power spectrum of the PC of the AMM patterns simulated by the model and from the observation, respectively. It is possible to see that the pattern simulated by BESM-OA2.5 shows, similarly to the observed one, a predominant periodicity at decadal timescales.

4.2.1.3 South Atlantic Convergence Zone

The South Atlantic Convergence Zone (SACZ) is characterized by an intense NW-SE oriented cloud band that extends from the Amazon Basin to the South Atlantic subtropics, mainly during austral summer (Nogués-Paegle and Mo, 1997; Carvalho et

al., 2004; de Oliveira Vieira et al., 2013). The formation of the SACZ has a strong influence on the precipitation over southeast South America and is considered, together with the convection activity over the Amazon Basin, the main component of the South American Monsoon System (Jones and Carvalho, 2002). The southern part of the SACZ usually lies over cooler SST (Grimm, 2003; Robertson and Mechoso, 2000). Chaves and Nobre (2004) suggests that the formation of SACZ over the ocean tend to block the solar radiation by clouds, cooling the SST beneath. AGCM are not able to simulate the precipitation over cooler SST caused by SACZ (Marengo et al., 2003; Nobre et al., 2006; Nobre et al., 2012), since such models tend to increase the precipitation over warmer SST, as an hydrostatic response. Nobre et al. (2012) has shown that coupled AOGCMs are able to simulate the SACZ formation over colder SST anomalies, as this class of models englobes the atmosphere-ocean surface thermodynamic coupling. Following Nobre et al. (2012), a correlation between seasonal precipitation and SST anomalies for the austral summer (DJF) over the tropical South Atlantic (40º S−10º N; 70º W−20º E) over the period 1979−2010 for observations and for the period 1971−2002 for the model, so 32 years are used. Figure 19 shows the rainfall-SST anomaly correlation maps for both BESM-OA2.5 and observations. BESM-OA2.5 are able to simulate an inverse correlation between precipitation and SST in the southeast of Brazil (near 20 °S), suggesting the capacity of simulating precipitation over cooler SST, a feature related to the formation of SACZ (that tends to cooler the SST). Its noteworthy in Figure 19 that BESM-OA2.5 is capable to generate both positive and negative SSTA-rainfall correlations over the equatorial Atlantic (positive, thermally direct driven circulation over the equatorial region and negative, thermally indirect driven atmospheric circulation over the SW tropical Atlantic, Figure 19a), a feature also

present in the observation correlation map of Figure 19b.

4.2.1.4 Madden-Julian Oscillation

The Madden-Julian Oscillation (MJO) is the prominent intraseasonal variability (30-90 days) over the eastern Indian and western Pacific tropical regions and consists on events of deep convection coupled to atmospheric circulation that packed propagate together through the equatorial region eastward (Madden and Julian, 1971, Madden and Julian, 1972; Zhang, 2005). The influence of MJO events with large-scale phenomena has been reported, as in the case of the evolution of ENSO (e.g. Takayabu et al., 1999), formation of tropical cyclones (e.g. Liebmann et al., 1994) or in the North Atlantic Oscillation (e.g. Lin et al., 2009). To evaluate the MJO simulated by the model it is performed the wavenumber-frequency power spectrum analysis for tropical (10 °S–10 °N) averaged daily outgoing long-wave radiation (OLR) and daily zonal wind component at 850 hPa pressure level (U850), for the boreal winter (Nov-Apr) over the period 1971–2000. To compute and plot the wavenumber-frequency power spectrum it is used the MJO Simulation Diagnostic package (details in Waliser et al., 2009).

Fig. 20a and Fig. 20b show the wavenumber-frequency power spectrum for OLR for BESM-OA2.5 and 20CRv2, respectively. Although BESM-OA2.5 presents an eastward propagating disturbance with wavenumber 1, it is characterized by lower frequency (> 80 days) compared to the maxima peak within 30–80 days frequency band shown by the 20CRv2, despite it spreads over lower frequencies than 80 days. This observed peak has more energy for wavenumber 2. A westward propagating disturbance (negative frequencies) with weaker energy than the eastward propagating counterpart appears in 20CRv2, with a peak for wavenumber 2. Similarly, BESM-OA2.5 also

shows a westward propagating disturbance with weaker energy for wavenumber 1–3. The wavenumber-frequency power spectrum for U850 in 20CRv2 shows an eastward propagating disturbance which peaks at the 30–80 days frequency band with wavenumber 1 (Fig. 20d). In the case of BESM-OA2.5 there is an eastward propagation with a periodicity slightly higher than 80 days for wavenumber 1 but this disturbance spreads over different frequencies out of the 30–80 days frequency band (Fig. 20c). It also presents a westward propagating disturbance that is absent in the Reanalysis. BESM-OA2.5 poorly simulates the MJO and underestimates its amplitude. However, MJO has been highlighted as a phenomenon that climate models struggle to simulate in a proper way, especially by underestimate OLR and representing a coherent eastward propagation (Kim et al., 2009; Ahn et al., 2017).

4.2.2 Extratropical Variability

4.2.2.1 North Atlantic Oscillation

The North Atlantic Oscillation (NAO) is a major atmospheric variability pattern occurring in the North Atlantic, which is characterized by the oscillation of the difference on the sea level pressure (SLP) between Iceland and Portugal (Wanner et al., 2001; Hurrel et al., 2003). NAO has a great impact in the Euro-Atlantic region (Hurrell et al., 2003; Hurrell and Deser, 2009), with the notable work of Namias (1972) relating droughts over the Northeast Brazil to NAO variations. Recent studies also show its teleconnections to the East Asia (e.g. Yu and Zhou, 2004; Wu et al., 2012). The NAO's influence on a rapid climate change in the Northern Hemisphere has been highlighted in (Delworth et al., 2016), which increases the importance of its correct simulation. Since NAO's largest amplitude of variation occurs mainly during the boreal winter, the

1   analysis here is centered on this season. The period used to perform the analyses is

2   1950−2005. The leading EOF of the SLP averaged for boreal winter season (DJF) in the

3   Euro-Atlantic region shows that the NAO is well simulated by BESM-OA2.5 (Fig. 21a),

4   simulating the NAO dipole centers and their amplitudes very similar to the observed

5   pattern (Fig. 21b). The variances explained by the leading EOF are also similar, 50.2 %

6   and 44 % for BESM-OA2.5 and Reanalysis, respectively. The spectral analysis of the

7   leading PCs shows that BESM-OA2.5 captures the ~2.5 years cycle on the time

8   variability but fails to capture the ~8 years cycle (Fig. 21c and 21d). It is interesting to

9   note that BESM-OA2.5 simulates a NAO spatial pattern, without capturing its low-

10 frequency variability. By analyzing the NAO variability, we consider that it is not

11 necessary to analyze the Northern Annular Mode (NAM), since both are manifestation

12 of same mode of variability (Hurrell and Deser, 2009).

13 **4.2.1.2 Pacific-North America Pattern**

14   Jointly, the NAO and the Pacific-North American pattern (PNA) are the

15 dominant atmospheric internal modes over the boreal hemisphere. The PNA is

16 characterized by four centers of high pressure anomalies in the North Pacific and North

17 America, respectively; over Hawaii, to the south of the Aleutian Islands, in the

18 intermountain region of North America, and in the Gulf Coast region of the U.S.A.,

19 representing the centers of action of a stationary wave train extending from the tropical

20 Pacific into North America (Wallace and Gutzler, 1981). It exerts a significant influence

21 on surface temperature and precipitation over North America (Leathers et al., 1991).

22 Some studies have shown that, although the PNA is an internal atmospheric variability

23 phenomena, it is influenced by other climate variabilities, as the ENSO and the Pacific

1   Decadal Oscillation (PDO) (see Straus and Shukla, 2002; Yu and Zwiers, 2007).

2   Similar to NAO, the PNA has its largest variation of amplitude during the boreal

3   winter; therefore, the present analysis is performed for this season. Following Wallace

4   and Gutzler (1981), we construct one-point correlation maps for BESM-OA2.5 and

5   20CRv2 Reanalysis in order to evaluate the capacity of the model to reproduce the PNA

6   pattern. The one-point correlation maps correlate 500 hPa geopotential height at the

7   reference point (45 ºN, 165 ºW) with all the other grid points of the map domain (0º−80º

8   N; 240º−70º W). The time series used to perform the correlations are averaged boreal

9   winter seasonal (DJF) dataset over the period 1950−2005. The time series are departed

10   from their long-term mean and normalized at each grid point prior the correlation

11   computation. Figure 22 shows the one-point correlation maps for BESM-OA2.5 (Fig.

12   22a) and 20CRv2 (Fig. 2b). In this figure, it is possible to check the four centers of

13   action simulated by the model, which shows a stronger correlation between the four

14   high pressure centers when compared with reanalysis correlation maps in Figure 22b.

15   **4.2.1.2 Pacific-South America Patterns**

16   The second and third EOF of 500 hPa geopotential height over the Southern

17   Hemisphere (20º−90º S) present a notable resemblance to the Pacific-South America

18   (PSA) teleconnection pattern (Mo and Peagle, 2001). PSA patterns are stationary

19   Rossby wave trains extending from central Pacific to Argentina, in which the PSA1

20   (EOF2) is a response to ENSO and the PSA2 (EOF3) is associated to the quasi-biennial

21   component of ENSO (Karoly, 1989; Mo and Peagle, 2001). These patterns have a

22   significant impact on rainfall anomalies over South America (Mo and Peagle, 2001).

23   Figure 23 shows the PSA patterns both simulated by BESM-OA2.5 and from

1   Reanalysis. As the explained variance of EOF2 and EOF3 are close, the EOFs seem to

2   degenerate for both Reanalysis and model simulation. In order to relax the orthogonality

3   constraint, it is performed a rotated EOF (REOF) retaining the first 10 modes. The

4   REOF2 and REOF3 resemble the EOF2 and EOF3 respectively, implying that they are

5   independent modes. The PSA pattern is well simulated by BESM-OA2.5, although the

6   model changes the order of the EOF patterns. BESM-OA2.5 shows an anomaly south of

7   South Africa (Fig. 23c) that does not appear in the Reanalysis (Fig. 23b). PSA patterns

8   have significant interannual and decadal variabilities (Zhang et al., 2016). PSA patterns

9   simulated by BESM-OA2.5 have only significant variability in the interannual scale,

10   with absent decadal variability (figure not shown).

11   **4.2.1.4 Southern Annular Mode**

12   The Southern Annular Mode (SAM) is the dominant atmospheric variability in

13   the Southern Hemisphere, occurring in the extra-tropics and in the high latitudes

14   (Kidson,1988). It is also referred to as Antarctic Oscillation (AAO; Gong and Wang,

15   1999). SAM variability is characterized by anomalies variation in the polar low-

16   pressure and in the surrounded zonally high-pressure belt. It can be captured through the

17   first EOF applied to different atmospheric variables, as the sea level pressure, different

18   geopotential height levels or the surface air temperature (Kidson, 1988; Rogers and van

19   Loon, 1982; Thompson and Wallace, 2000). To evaluate the capacity of BESM-OA2.5

20   to simulate this atmospheric mode of variability, EOF analysis is applied to the monthly

21   mean 500 hPa geopotential height field from 20 °S to 90 °S, over the period 1950−2005,

22   for both model and Reanalysis. The SAM pattern simulated by BESM-OA2.5 resembles

23   very well the observed pattern, with the mid-latitude 500 hPa geopotential height

variation centers depicted in the same longitudes as observations, but with differences in

the amplitude values (Fig. 24). However, the explained variance is higher compared

with observation. The explained variances of BESM-OA2.5 and 20CRv2 are 34.1 %

and 21.0 %, respectively. The SAM is a quasi-decadal mode of variability (see Yuan

and Yonekura, 2011), however the BESM-OA2.5 power spectrum reveals a SAM with

a markedly interannual variability, without the peak between 8 and 16 years as obtained

in the Reanalysis (figure not shown).

4.2.1.5 Pacific Decadal Oscillation

Observed SST anomalies over the North Pacific have shown an oscillatory

pattern in the central and western parts in relation to the tropical part and along the

North American west coast. This oscillatory shift of SST anomalies with interdecadal

periodicity was termed Pacific Decadal Oscillation (PDO) and it is defined as the

leading EOF of the monthly SST anomalies over North Pacific (Mantua et al., 1997).

The positive phase of PDO is defined when negative SST anomalies predominate over

the central and western parts of North Pacific, and positive SST anomalies predominate

over the Tropical Pacific and along the North American west coast; being the negative

phase the reverse pattern. Many studies have connected the PDO with variations on

precipitation regimes in different regions around the world, as South China monsoon

(e.g. Wu and Mao, 2016), Indian monsoon (e.g. Krishnamurthy and Krishnamurthy,

2016) and together with ENSO in the precipitation regime in North America (see Hu

and Huang, 2009). There are different mechanisms that modulate PDO, in which one of

them is the response of the Northern Pacific SST to the ENSO variability via the

"atmospheric bridge" (for a detailed review, see Newman et al., 2016).

Following the definition (Mantua et al., 1997), the spatial pattern of PDO is obtained by regressing the SST anomalies onto the leading normalized PC time series, shown in Figure 24 which in this case is showing the positive phase of the PDO. The EOF is applied to monthly SST anomalies over North Pacific (20º−60º N; 240º−110º W) over the period 1900−2005. BESM-OA2.5 is not capable of reproducing this pattern by the leading EOF. The PDO pattern only appears on the second EOF (Fig. 25a), with the explained variance of 14.0 % against 20.5 % of observations. Although the EOF2 resembles the PDO mode, the tropical part has a weaker variation than the observation. The reason of incapacity of the model in reproducing the PDO as the leading mode of variability is probably due to the model's simulation of weaker ENSO variability, both in spatial and temporal scales. These deficiencies may impact the mechanisms that reproduce the PDO, mainly via the "atmospheric bridge" as referred earlier. Figures 26a and 26b show the normalized PC2 and PC1 time series of BESM-OA2.5 and ERSSTv4, respectively. It is possible to note that both time series present a multidecadal periodicity, but in different time scales as it is confirmed by the power spectrum (Fig. 26c and 26d). The power spectrum shows that both time series present interannual periodicity (~5-6 years), with BESM-OA2.5 multidecadal variability strongest spectrum around 15 years, a higher frequency compared with observation (~22 and ~40-45 years).

5. Summary

The capacity of Earth System Models to project a future climate under the conditions given by future scenarios of atmospheric greenhouse gas concentrations can

be assessed by how accurate these models are able to reproduce observed climate features. Therefore, the evaluation of how these models perform for the historical period when there are observations to compare with model's calculations represents a key part of the Earth System modelling. In this study, BESM-OA2.5 historical simulation is evaluated for the period 1850−2005 following the CMIP5 protocol (Taylor et al., 2012) with focus on simulations of its mean climate and key large-scale modes of climate variability.

BESM-OA2.5 is an updated version of BESM-OA2.3 (Nobre et al. 2013; Giarolla et al. 2015) regarding the atmospheric model, which consists in the new Brazilian Global Atmospheric Model (BAM; Figueroa et al., 2016). This new version allowed to alleviate a mean global bias of energy balance at the top of the atmosphere of -20 W m^{-2} to -4 W m^{-2}.Moreover, systematic errors were reduced in wind, humidity and temperature in the surface layer over oceanic regions by the inclusion formulations presented by Jiménez et al. (2012).

The analysis of the mean climate shows that the model is able to simulate the general mean climate state. Nevertheless, some significant biases appear at the simulation, as a double ITCZ over the Pacific and Atlantic Oceans, some notable regional biases in the precipitation field (e.g., over the Amazon and Indian regions) and in the SST field (e.g., south of Greenland). Yet, the model has shown an improvement in simulating the ITCZ and a reduction in the global precipitation RMSE compared with BESM-OA version 2.3. BESM-OA2.5 shows an almost globally positive SST bias, which did not occur in version 2.3, however the SST RMSE was slightly reduced in the newer version of the model.

1   The most relevant climate patterns on interannual to decadal time scales

2   simulated by BESM-OA2.5 are compared with the ones obtained from observations and

3   Reanalysis. Over the Pacific, the ENSO is simulated with lower amplitude of variability

4   than the observations and such weak ENSO seems to impact other Pacific variability

5   patterns such as the PDO. Conversely, the major phenomena on the Atlantic basin are

6   well represented in BESM-OA2.5 simulations. This is the case for the Tropical Atlantic

7   mode of interhemispheric variability (AMM) that is very well simulated by the model in

8   term of the spatial pattern and temporal variability. It is worth to note that this mode is

9   considered poorly simulated by the models used in the Intergovernmental Panel on

10   Climate Change (IPCC) fifth assessment report (AR5) (Flato et al., 2013). It is also

11   relevant to highlight BESM-OA2.5 ability to represent the enhanced rainfall over cooler

12   waters over the SW Tropical Atlantic, associated with the South Atlantic Convergence

13   Zone (SACZ). The capacity of the model in simulating the AMM and SACZ is an

14   important result since one of the main aims is the representation of modes that directly

15   impacts the precipitation over South America. The AMOC reproduced by BESM-

16   OA2.5 has the meridional overturning structure comparable with the ensemble AMOC

17   simulated by the CMIP5's models. BESM's maximum AMOC strength average value is

18   slighter lower than the average value that has been observed by the project RAPID, but

19   well within the range of mean square root variability that is observed. Although the

20   averaged maximum strength AMOC simulated by the CMIP5 models is within the

21   mean range square root variability that is observed, most models tend to simulate strong

22   AMOC, with a maximum strength above 20 Sv, and out of the range (Zhang and Wang,

23   2013). The NAO atmospheric variability, which is well simulated by the CMIP5 models

24   (Ning and Bradley, 2016) is also very well simulated by BESM-OA2.5. In the extra-

tropics, BESM-OA2.5 is capable to reproduce fairly well majors variabilities in both Hemispheres, as the PNA, PSA, and the SAM teleconnections patterns, comparable to CMIP5 models that reproduce the PNA (Ning and Bradley, 2016) and the SAM (Zheng et al. 2013).

Similarly to Nobre et al. (2013), this study aims to evaluate the BESM-OA2.5 by comparing the most important features of the climate system simulated by the model with observations and Reanalysis. The next version of the model (BESM-OA2.8) is already under development. In this new version, the MOM4p1 ocean model has been replaced by the MOM5. Regarding the atmospheric model, new developments have been carried out to improve BAM's capacity, being the most important the inclusion of a scheme of humidity in the planetary boundary layer, a new dynamic core and new cloud cover scheme (Figueroa et al., 2016). This new version of BESM carries the challenges of improving the simulation of the precipitation, in particular to alleviate the deficit over the Amazon. The ENSO is the large-scale phenomenon that will receive a scrutiny in order to understand the reasons for a weak variability. The other feature of the model is the weaker warming under the CO_2 equivalent only forcing, relative to other CMIP5 that do not consider the direct and indirect effects of atmospheric aerosols. Assuming that BESM-OA2.5 should respond consistently with CMIP5 models, it would underestimate the warming observed in the last decades. However, models can respond in different ways to external forcing, therefore, in the near future, the aim is to carry out a numerical experiment in which the model is forced with observed estimate of aerosol concentration (as read-in field) in order to address to what extension BESM is impacted. In the future, a study comparing the versions 2.5 and 2.8 of the BESM-OA is aimed in

order to fully report the advances of the modeling work developed in the last couple years. Such a study will give a broader perspective of the technical challenges overcome throughout this project and assess the improvements achieved in each version of the model in simulating the climate system.

Code and data availability

The BESM-OA2.5 source code is freely available after signature of a license agreement. Please contact Paulo Nobre to obtain the source code and data of BESM-OA2.5.

Competing interests

There are no competing interests of which the authors are aware.

Acknowledgements

This research was partially funded by FAPESP (2009/50528-6), FAPESP (2008/57719-9) and by the National Institute of S&T for Climate Change (CNPq 573797/2008-0). SFV is supported by a Ph.D. grant funded by CAPES. MBJ is supported by a grant funded by FAPESP (2018/06204-0). The authors would like to acknowledge Rede CLIMA, FAPESP and INPE for the use of its supercomputer facility, which made this

work possible. Twentieth Century Reanalysis Project data sets (20CRv2) are provided by the U.S. Department of Energy, Office of Science Innovative and Novel Computational Impact on Theory and Experiment (DOE INCITE) program, and Office of Biological and Environmental Research (BER), and by the National Oceanic and Atmospheric Administration Climate Program Office. The GPCP combined precipitation data sets were developed and computed by the NASA/Goddard Space Flight Center's Mesoscale Atmospheric Processes Laboratory. The HadCRUT4 data sets are provided by the Met Office Hadley Centre and the University of East Anglia/Climatic Research Unit. The ISCCP D2 data sets are provided through the International Satellite Cloud Climatology Project, maintained by the ISCCP research group at the NASA/Goddard Institute for Space Studies. The Extended Reconstructed Sea Surface Temperature (ERSSTv4) is provided by the NOAA/OAR/ESRL/PSD. Data from the RAPID-WATCH MOC monitoring project are funded by the Natural Environment Research Council. The authors acknowledge the World Climate Research Programme's Working Group on Coupled Modelling, which is responsible for CMIP, and we thank the climate modeling groups (listed in Table 1 of this paper) for producing and making available their model output. For CMIP the U.S. Department of Energy's Program for Climate Model Diagnosis and Intercomparison provides coordinating support and led development of software infrastructure in partnership with the Global Organization for Earth System Science Portals. This work is part of the Ph.D. thesis of SFV under the guidance of CN and PN.

References

Adler, R. F., Huffman, G. J., Chang, A., Ferraro, R., Xie, P.-P., Janowiak, J., Rudolf, B., Schneider, U., Curtis, S., Bolvin, D., Gruber, A., Susskind, J., Arkin, P. and Nelkin, E.: The Version-2 Global Precipitation Climatology Project (GPCP) Monthly Precipitation Analysis (1979–Present), J. Hydrometeorol., 4(6), 1147–1167, doi:10.1175/1525-7541(2003)004<1147:TVGPCP>2.0.CO;2, 2003.

Anthes, R. A.: A Cumulus Parameterization Scheme Utilizing a One-Dimensional Cloud Model, Mon. Weather Rev., 105(3), 270–286, doi:10.1175/1520-0493(1977)105<0270:ACPSUA>2.0.CO;2, 1977.

Ahn, M. S., Kim, D., Sperber, K. R., Kang, I. S., Maloney, E., Waliser, D. and Hendon, H.: MJO simulation in CMIP5 climate models: MJO skill metrics and process-oriented diagnosis, Clim. Dyn., 49(11–12), 4023–4045, doi:10.1007/s00382-017-3558-4, 2017.

Arakawa, A. and Schubert, W. H.: Interaction of a Cumulus Cloud Ensemble with the Large-Scale Environment, Part I, J. Atmos. Sci., 31(3), 674–701, doi:10.1175/1520-0469(1974)031<0674:IOACCE>2.0.CO;2, 1974.

Bentsen, M., Bethke, I., Debernard, J. B., Iversen, T., Kirkevåg, A., Seland, Ø., Drange, H., Roelandt, C., Seierstad, I. A., Hoose, C. and Kristjánsson, J. E.: The Norwegian Earth System Model, NorESM1-M − Part 1: Description and basic evaluation of the physical climate, Geosci. Model Dev., 6(3), 687–720, doi:10.5194/gmd-6-687-2013, 2013.

Bottino, M. J., and Nobre, P.: Impacts of cloud cover schemes on the Atlantic climate in the Brazilian Earth System Model − BESM-OA2.3. (Submitted to Climate Dynamics).

Buckley, M. W. and Marshall, J.: Observations, inferences, and mechanisms of the Atlantic Meridional Overturning Circulation: A review, Rev. Geophys., 54, 5–63, doi:10.1002/2015RG000493.Received, 2015.

Cao, J., Wang, B., Yang, Y.-M., Ma, L., Li, J., Sun, B., Bao, Y., He, J., Zhou, X. and Wu, L.: The NUIST Earth System Model (NESM) version3: description and preliminary evaluation, Geosci. Model Dev., 11(7), 2975–2993, doi:10.5194/gmd-11-2975-2018, 2018.

Capistrano, V. B., Nobre, P., Tedeschi, R., Silva, J., Bottino, M., da Silva Jr., M. B., Menezes Neto, O. L., Figueroa, S. N., Bonatti, J. P., Kubota, P. Y., Reyes Fernandez, J. P., Giarolla, E., Vial, J., and Nobre, C. A.: Overview of climate change in the BESM-OA2.5 climate model, Geosci. Model Dev. Discuss., https://doi.org/10.5194/gmd-2018-209, in review, 2018.

Carvalho, L. M. V, Jones, C. and Liebmann, B.: The South Atlantic convergence zone: Intensity, form, persistence, and relationships with intraseasonal to interannual activity and extreme rainfall, J. Clim., 17(1), 88–108, doi:10.1175/1520-0442(2004)017<0088:TSACZI>2.0.CO;2, 2004.

Chang, P., Ki, L. and Li, H.: A decadal climate variation in the tropical Atlantic Ocean from thermodynamic air-sea interactions, Nature, 385(6), 516–518, 1997.

Charlton-Perez, A. J., Baldwin, M. P., Birner, T., Black, R. X., Butler, A. H., Calvo, N., Davis, N. A., Gerber, E. P., Gillett, N., Hardiman, S., Kim, J., Krüger, K., Lee, Y. Y., Manzini, E., McDaniel, B. A., Polvani, L., Reichler, T., Shaw, T. A., Sigmond, M., Son, S. W., Toohey, M., Wilcox, L., Yoden, S., Christiansen, B., Lott, F., Shindell, D., Yukimoto, S. and Watanabe, S.: On the lack of stratospheric dynamical variability in low-top versions of the CMIP5 models, J. Geophys. Res. Atmos., 118(6), 2494–2505, doi:10.1002/jgrd.50125, 2013.

Chaves, R. R. and Nobre, P.: Interactions between sea surface temperature over the South Atlantic Ocean and the South Atlantic Convergence Zone, Geophys. Res. Lett., 31(3), 1–4, doi:10.1029/2003GL018647, 2004.

Cheng, W., Chiang, J. C. H. and Zhang, D.: Atlantic meridional overturning circulation (AMOC) in CMIP5 Models: RCP and historical simulations, J. Clim., 26(18), 7187–7197, doi:10.1175/JCLI-D-12-00496.1, 2013.

Chiang, J. C. H. and Vimont, D. J.: Analogous Pacific and Atlantic Meridional Modes of Tropical Atmosphere – Ocean Variability, J. Clim., 17, 4143–4158, doi:10.1175/JCLI4953.1, 2004.

Chou, M.-D. and Suarez, M. J.: A solar radiation parame- terization (CLIRAD-SW) for atmospheric studies. NASA Tech. Memo NASA/TM-1999-104606, 40 pp., 1999.

Chou, S. C., Lyra, A., Mourão, C., Dereczynski, C., Pilotto, I., Gomes, J., Bustamante, J., Tavares, P., Silva, A., Rodrigues, D., Campos, D., Chagas, D., Sueiro, G., Siqueira, G., Nobre, P. and Marengo, J.: Evaluation of the Eta Simulations Nested in Three Global Climate Models, Am. J. Clim. Chang., 3(5), 438–454, doi:10.4236/ajcc.2014.35039, 2014.

Compo, G. P., Whitaker, J. S., Sardeshmukh, P. D., Matsui, N., Allan, R. J., Yin, X., Gleason, B. E., Vose, R. S., Rutledge, G., Bessemoulin, P., BroNnimann, S., Brunet, M., Crouthamel, R. I., Grant, A. N., Groisman, P. Y., Jones, P. D., Kruk, M. C., Kruger, A. C., Marshall, G. J., Maugeri, M., Mok, H. Y., Nordli, O., Ross, T. F., Trigo, R. M., Wang, X. L., Woodruff, S. D. and Worley, S. J.: The Twentieth Century Reanalysis Project, Q. J. R. Meteorol. Soc., 137(654), 1–28, doi:10.1002/qj.776, 2011.

Delworth, T. L. and Mann, M. E.: Observed and simulated multidecadal variability in the Northern Hemisphere, Clim. Dyn., 16(9), 661–676, doi:10.1007/s003820000075, 2000.

Delworth, T. L., Zeng, F., Vecchi, G. A., Yang, X., Zhang, L. and Zhang, R.: The North Atlantic Oscillation as a driver of rapid climate change in the Northern Hemisphere, Nat. Geosci., 9(7), 509–512, doi:10.1038/ngeo2738, 2016.

Dijkstra, H. A.: The ENSO phenomenon: theory and mechanisms, Adv. Geosci., 6, 3–15, doi:10.5194/adgeo-6-3-2006, 2006.

Enfield, D. B., Mestas-Nuñez, A. M. and Trimble, P. J.: The Atlantic multidecadal oscillation and its relation to rainfall and river flows in the continental U.S, Geophys. Res. Lett., 28(10), 2077–2080, doi:10.1029/2000GL012745, 2001.

Ferrier, B. S., Jin, Y., Lin, Y., Black, T., Rogers, E. and DiMego, G.: Implementation of a 527 new grid-scale cloud and precipitation scheme in the NCEP Eta model. Amer. Meteor. Soc., 280–283, 2002.

Figueroa, S. N., Bonatti, J. P., Kubota, P. Y., Grell, G. A., Morrison, H., Barros, S. R. M., Fernandez, J. P. R., Ramirez, E., Capistrano, V. B., Alvim, D. S., Enoré, D. P., Diniz, F. L. R., Barbosa, H. M. J., Mendes, C. L. and Panetta, J.: The Brazilian Global Atmospheric Model (BAM): Performance for Tropical Rainfall Forecasting and Sensitivity to Convective Scheme and Horizontal Resolution, Weather Forecast., 31(5), 1547–1572, doi:10.1175/WAF-D-16-0062.1, 2016.

Flato, G. M.: Earth system models: An overview, Wiley Interdiscip. Rev. Clim. Chang., 2(6), 783–800, doi:10.1002/wcc.148, 2011.

Flato, G., J. Marotzke, B. Abiodun, P. Braconnot, S.C. Chou, W. Collins, P. Cox, F. Driouech, S. Emori, V. Eyring, C. Forest, P. Gleckler, E. Guilyardi, C. Jakob, V. Kattsov, C. Reason and M. Rummukainen, 2013: Evaluation of Climate Models. In: Climate Change 2013: The Physical Science Basis. Contribution of Working Group I to the Fifth Assessment Report of the Intergovernmental Panel on Climate Change [Stocker, T.F., D. Qin, G.-K. Plattner, M. Tignor, S.K. Allen, J. Boschung, A. Nauels, Y. Xia, V. Bex and P.M. Midgley (eds.)]. Cambridge University Press, Cambridge, United Kingdom and New York, NY, USA.

Gent, P. R., Danabasoglu, G., Donner, L. J., Holland, M. M., Hunke, E. C., Jayne, S. R., Lawrence, D. M., Neale, R. B., Rasch, P. J., Vertenstein, M., Worley, P. H., Yang, Z.-L., Zhang, M.: The Community Climate System Model Version 4, J. Clim., 24(19), 4973–4991, doi:10.1175/2011JCLI4083.1, 2011.

Giarolla, E., Siqueira, L. S. P., Bottino, M. J., Malagutti, M., Capistrano, V. B. and Nobre, P.: Equatorial Atlantic Ocean dynamics in a coupled ocean atmosphere model simulation, Ocean Dyn., 65(6), 831–843, doi:10.1007/s10236-015-0836-8, 2015.

Gong, D. and Wang, S.: Definition of Antarctic Oscillation Index, Geophys. Res. Lett., 26(4), 459–462, doi:10.1029/1999GL900003, 1999. Grell, G. and Dévényi, D. A.: A generalized approach to parameterizing convection combining ensemble and data assimilation techniques, Geophys. Res. Lett., 29(14), 10–13, doi:10.1029/2002GL015311, 2002.

Griffies, S. M.: Elements of MOM4p1. NOAA/Geophysical Fluid Dynamics Laboratory Ocean Group Tech. Rep. 6, 444 pp., 2009.

Grimm, A. M.: The El Niño impact on the summer monsoon in Brazil: Regional processes versus remote influences, J. Clim., 16(2), 263–280, doi:10.1175/1520-0442(2003)016<0263:TENIOT>2.0.CO;2, 2003.

Harshvardhan, Davies, R., Randall, D. A. and Corsetti, T. G.: A fast radiation parameterization for atmospheric circulation models, J. Geophys. Res., 92(D1), 1009–1016, doi:10.1029/JD092iD01p01009, 1987.

Hu, Z. Z. and Huang, B.: Interferential impact of ENSO and PDO on dry and wet conditions in the U.S. great plains, J. Clim., 22(22), 6047–6065, doi:10.1175/2009JCLI2798.1, 2009.

Huang, B., Banzon, V. F., Freeman, E., Lawrimore, J., Liu, W., Peterson, T. C., Smith, T. M., Thorne, P. W., Woodruff, S. D. and Zhang, H. M.: Extended reconstructed sea surface temperature version 4 (ERSST.v4). Part I: Upgrades and intercomparisons, J. Clim., 28(3), 911–930, doi:10.1175/JCLI-D-14-00006.1, 2015.

Huffman, G. J., Adler, R. F., Bolvin, D. T. and Gu, G.: Improving the global precipitation record: GPCP Version 2.1, Geophys. Res. Lett., 36(17), L17808, doi:10.1029/2009GL040000, 2009.

Hurrell, J. W. and Deser, C.: North Atlantic climate variability: The role of the North Atlantic Oscillation, J. Mar. Syst., 78(1), 28–41, doi:10.1016/j.jmarsys.2008.11.026, 2009.

Hurrell, J. W., Kushnir, Y., Otterson, G. and Visbeck, M.: An Overview of the North Atlantic Oscillation, North Atl. Oscil. Clim. Significance Environ. Impact, 134, 263, doi:10.1029/GM134, 2003.

Hwang, Y.-T. and Frierson, D. M. W.: Link between the double-Intertropical Convergence Zone problem and cloud biases over the Southern Ocean., Proc. Natl. Acad. Sci. U. S. A., 110(13), 4935–40, doi:10.1073/pnas.1213302110, 2013.

Ji, D., Wang, L., Feng, J., Wu, Q., Cheng, H., Zhang, Q., Yang, J., Dong, W., Dai, Y., Gong, D., Zhang, R. H., Wang, X., Liu, J., Moore, J. C., Chen, D. and Zhou, M.: Description and basic evaluation of Beijing Normal University Earth System Model (BNU-ESM) version 1, Geosci. Model Dev., 7(5), 2039–2064, doi:10.5194/gmd-7-2039-2014, 2014.

Jiménez, P. A., Dudhia, J., González-Rouco, J. F., Navarro, J., Montávez, J. P. and García-Bustamante, E.: A Revised Scheme for the WRF Surface Layer Formulation, Mon. Weather Rev., 140(3), 898–918, doi:10.1175/MWR-D-11-00056.1, 2012.

Jones, C. and Carvalho, L. M. V: Active and break phases in the South American monsoon system, J. Clim., 15(8), 905–914, doi:10.1175/1520-0442(2002)015<0905:AABPIT>2.0.CO;2, 2002.

Karoly, D. J.: Southern Hemisphere Circulation Features Associated with El-Nino-Southern Oscillation Events, J. Clim., 2, 1239–1252, doi: 10.1175/1520-0442(1989)002<1239:SHCFAW>2.0.CO;2., 1989.

Kidson, J. W.: Interannual Variations in the Southern Hemisphere Circulation, J. Clim., 1(12), 939–953, doi:10.1175/1520-0442(1988)001<1177:IVITSH>2.0.CO;2, 1988.

Kim, D., Sperber, K., Stern, W., Waliser, D., Kang, I. S., Maloney, E., Wang, W., Weickmann, K., Benedict, J., Khairoutdinov, M., Lee, M. I., Neale, R., Suarez, M., Thayer-Calder, K. and Zhang, G.: Application of MJO simulation diagnostics to climate models, J. Clim., 22(23), 6413–6436, doi:10.1175/2009JCLI3063.1, 2009.

Krishnamurthy, L. and Krishnamurthy, V.: Indian monsoon' s relation with the decadal part of PDO in observations and NCAR CCSM4, Int. J. Climatol., doi:10.1002/joc.4815, 2016.

Large, W. G. and Yeager, S. G.: The global climatology of an interannually varying air - Sea flux data set, Clim. Dyn., 33(2–3), 341–364, doi:10.1007/s00382-008-0441-3, 2009.

Leathers, D. J., Yarnal, B., Palecki, M. A., Leathers, D. J., Yarnal, B. and Palecki, M. A.: The Pacific/North American Teleconnection Pattern and United States Climate. Part I: Regional Temperature and Precipitation Associations, J. Clim., 4(5), 517–528, doi:10.1175/1520-0442(1991)004<0517:TPATPA>2.0.CO;2, 1991.

Levitus, S.: Climatological Atlas of the World Ocean.NOAA Prof. Paper 13, 173 pp. and 17 microfich, 1982.

Li, G. and Xie, S. P.: Tropical biases in CMIP5 multimodel ensemble: The excessive equatorial pacific cold tongue and double ITCZ problems, J. Clim., 27(4), 1765–1780, doi:10.1175/JCLI-D-13-00337.1, 2014.

Liebmann, B., Hendon, H. H. and Glick, J. D.: The Relationship Between Tropical Cyclones of the Western Pacific and Indian Oceans and the Madden-Julian Oscillation, J. Meteorol. Soc. Japan. Ser. II, 72(3), 401–412, doi:10.2151/jmsj1965.72.3_401, 1994.

Lin, H., Brunet, G. and Derome, J.: An observed connection between the North Atlantic oscillation and the Madden-Julian oscillation, J. Clim., 22(2), 364–380, doi:10.1175/2008JCLI2515.1, 2009.

Lu, R., Dong, B. and Ding, H.: Impact of the Atlantic Multidecadal Oscillation on the Asian summer monsoon, Geophys, Res. Lett., 33, L24701, doi(24), 101029/, doi:10.1029/2006GL027655, 2006.

Lumpkin, R. and Speer, K.: Global Ocean Meridional Overturning, J. Phys. Oceanogr., 37(10), 2550–2562, doi:10.1175/JPO3130.1, 2007.

Lutz, K., Jacobeit, J. and Rathmann, J.: Atlantic warm and cold water events and impact on African west coast precipitation, Int. J. Climatol., 35(1), 128–141, doi:10.1002/joc.3969, 2015.

Madden, R. A. and Julian, P. R.: Detection of a 40–50 Day Oscillation in the Zonal Wind in the Tropical Pacific, J. Atmos. Sci., 28(5), 702–708, doi:10.1175/1520-0469(1971)028<0702:DOADOI>2.0.CO;2, 1971.

Madden, R. A. and Julian, P. R.: Description of Global-Scale Circulation Cells in the Tropics with a 40–50 Day Period, J. Atmos. Sci., 29(6), 1109–1123, doi:10.1175/1520-0469(1972)029<1109:DOGSCC>2.0.CO;2, 1972.

Mantua, N. J., Hare, S. R., Zhang, Y., Wallace, J. M. and Francis, R. C.: A Pacific Interdecadal Climate Oscillation with Impacts on Salmon Production, Bull. Am. Meteorol. Soc., 78(6), 1069–1079, doi:10.1175/1520-0477(1997)078<1069:APICOW>2.0.CO;2, 1997.

Marengo, J. A., Calvalcanti, I. F. A., Satyamurty, P., Trosnikov, I., Nobre, C. A., Bonatti, J. P., Camargo, H., Sampaio, G., Sanches, M. B., Manzi, A. O., Castro, C. A. C., D'Almeida, C., Pezzi, L. P. and Candido, L.: Assessment of regional seasonal rainfall predictability using the CPTEC/COLA atmospheric GCM, Clim. Dyn., 21(5–6), 459–475, doi:10.1007/s00382-003-0346-0, 2003.

Menary, M. B., Kuhlbrodt, T., Ridley, J., Andrews, M. B., Dimdore-Miles, O. B., Deshayes, J. et al.: Preindustrial control simulations with HadGEM3-GC3.1 for CMIP6., J. Adv. Model. Earth Syst., 10, 3049–3075, doi:https://doi.org/10.1029/2018MS001495, 2018.

McCarthy, G. D., Smeed, D. A., Johns, W. E., Frajka-Williams, E., Moat, B. I., Rayner, D., Baringer, M. O., Meinen, C. S., Collins, J. and Bryden, H. L.: Measuring the Atlantic Meridional Overturning Circulation at 26 N, Prog. Oceanogr., 130, 91–111, doi:10.1016/j.pocean.2014.10.006, 2015.

McPhaden, M. J., Zebiak, S. E. and Glantz, M. H.: ENSO as an integrating concept in earth science, Science, 314(5806), 1740–1745, doi:10.1126/science.1132588, 2006.

Meehl, G. A., Moss, R., Taylor, K. E., Eyring, V., Stouffer, R. J., Bony, S. and Stevens, B.: Climate model intercomparisons: Preparing for the next phase, Eos, 95(9), 77–78, doi:10.1002/2014EO090001, 2014.

Mellor, G. L. and Yamada, T.: Development of a turbulence closure model for geophysical fluid problems, Rev. Geophys., 20(4), 851–875, doi:10.1029/RG020i004p00851, 1982.

Mo, K. C. and Peagle, J. N.: The Pacific-South American modes and their downstream effects, Int. J. Climatol, 21(10), 1211–1229, doi:10.1002/joc.685, 2001.

Morice, C. P., Kennedy, J. J., Rayner, N. A. and Jones, P. D.: Quantifying uncertainties in global and regional temperature change using an ensemble of observational estimates: The HadCRUT4 data set, J. Geophys. Res. Atmos., 117(8), 1–22, doi:10.1029/2011JD017187, 2012.

Newman, M., Alexander, M. A., Ault, T. R., Cobb, K. M., Deser, C., Di Lorenzo, E., Mantua, N. J., Miller, A. J., Minobe, S., Nakamura, H., Schneider, N., Vimont, D. J., Phillips, A. S., Scott, J. D. and Smith, C. A.: The Pacific decadal oscillation, revisited, J. Clim., 29(12), 4399–4427, doi:10.1175/JCLI-D-15-0508.1, 2016.

Ning, L. and Bradley, R. S.: NAO and PNA influences on winter temperature and precipitation over the eastern United States in CMIP5 GCMs, Clim. Dyn., 46(3–4), 1257–1276, doi:10.1007/s00382-015-2643-9, 2016.

Nobre, P., Shukla. J.: Variation of Sea surface Temperature, Wind Stress, and Rainfall over the Tropical Atlantic and South America, J. Clim., 9, 2464–2479, doi:http://dx.doi.org/10.1175/1520-0442(1996)009<2464:VOSSTW>2.0.CO;2, 1996.

Nobre, P., Marengo, J. A., Cavalcanti, I. F. A., Obregon, G., Barros, V., Camilloni, I., Campos, N. and Ferreira, A. G.: Seasonal-to-decadal predictability and prediction of South American climate, J. Clim., 19(23), 5988–6004, doi:10.1175/JCLI3946.1, 2006.

Nobre, P., De Almeida, R. A., Malagutti, M. and Giarolla, E.: Coupled ocean-atmosphere variations over the South Atlantic Ocean, J. Clim., 25(18), 6349–6358, doi:10.1175/JCLI-D-11-00444.1, 2012.

Nobre, P., Siqueira, L. S. P., De Almeida, R. A. F., Malagutti, M., Giarolla, E., Castel ã O, G. P., Bottino, M. J., Kubota, P., Figueroa, S. N., Costa, M. C., Baptista, M., Irber, L. and Marcondes, G. G.: Climate simulation and change in the brazilian climate model, J. Clim., 26(17), 6716–6732, doi:10.1175/JCLI-D-12-00580.1, 2013.

Nogu és-Paegle, J. and Mo, K. C.: Alternating Wet and Dry Conditions over South America during Summer, Mon. Weather Rev., 125, 279–291, doi:10.1175/1520-0493(1997)125<0279:AWADCO>2.0.CO;2, 1997.

Obukhov, A. M.: Turbulence in an atmosphere with a non-uniform temperature, Boundary-Layer Meteorol., 2(1), 7–29, doi:10.1007/BF00718085, 1971.

de Oliveira Vieira, S., Satyamurty, P. and Andreoli, R. V.: On the South Atlantic Convergence Zone affecting southern Amazonia in austral summer, Atmos. Sci. Lett., 14(1), 1–6, doi:10.1002/asl2.401, 2013.

Palmer, T. N., Doblas-Reyes, F. J., Weisheimer, A. and Rodwell, M. J.: Toward seamless prediction: Calibration of climate change projections using seasonal forecasts, Bull. Am. Meteorol. Soc., 89(4), 459–470, doi:10.1175/BAMS-89-4-459, 2008.

Richter, I.: Climate model biases in the eastern tropical oceans: Causes, impacts and ways forward, Wiley Interdiscip. Rev. Clim. Chang., 6(3), 345–358, doi:10.1002/wcc.338, 2015.

Richter, I., Xie, S. P., Behera, S. K., Doi, T. and Masumoto, Y.: Equatorial Atlantic variability and its relation to mean state biases in CMIP5, Clim. Dyn., 42(1–2), 171–188, doi:10.1007/s00382-012-1624-5, 2014.

Robertson, A. and Mechoso, C.: Interannual and interdecadal variability of the South Atlantic Convergence Zone, Mon. Weather Rev., 128(8), 2947–2957, doi:10.1175/1520-0493(2000)128<2947:IAIVOT>2.0.CO;2, 2000.

Rogers, J. C. and van Loon, H.: Spatial Variability of Sea Level Pressure and 500 mb Height Anomalies over the Southern Hemisphere, Mon. Weather Rev., 110(10), 1375–1392, doi:10.1175/1520-0493(1982)110<1375:SVOSLP>2.0.CO;2, 1982.

Rossow, W. B. and Schiffer, R. a: Advances in Understanding Clouds from ISCCP, Bull. Amer. Meteor. Soc., 80(11), 2261–2287, doi:10.1175/1520-0477(1999)080<2261:AIUCFI>2.0.CO;2, 1999.

von Storch, H.: Climate models and modeling: an editorial essay, Wiley Interdiscip. Rev. Clim. Chang., 1(3), 305–310, doi:10.1002/wcc.12, 2010.

Straus, D. M. and Shukla, J.: Does ENSO force the PNA?, J. Clim., 15(17), 2340–2358, doi:10.1175/1520-0442(2002)015<2340:DEFTP>2.0.CO;2, 2002.

Sutton, R. T. and Hodson, D. L. R.: Atlantic Ocean Forcing of North American and European Summer Climate, Science, 309(5731), 115–118, doi:10.1126/science.1109496, 2005.

Swapna, P., Krishnan, R., Sandeep, N., Prajeesh, A. G., Ayantika, D. C., Manmeet, S. and Vellore, R.: Long-Term Climate Simulations Using the IITM Earth System Model (IITM-ESMv2) With Focus on the South Asian Monsoon, J. Adv. Model. Earth Syst., 10(5), 1127–1149, doi:10.1029/2017MS001262, 2018.

Takayabu, Y. N., Iguchl, T., Kachi, M., Shibata, A. and Kanzawa, H.: Abrupt

termination of the 1997-98 El Nino in response to a Madden-Julian oscillation, Nature, 402(6759), 279–282, doi:10.1038/46254, 1999.

Tarasova, T. A., Barbosa, H. M. J. and Figueroa, S. N.: In- corporation of new solar radiation scheme into CPTECGCM. Instituto Nacional de Pesquisas Espaciais Tech. Rep. INPE- 14052-NTE/371, 44 pp. [Available online at http://mtc-m15. sid.inpe.br/col/sid.inpe.br/iris%401915/2006/01.16.10.40/doc/publicacao.pdf, 2006.

Tian, B.: Spread of model climate sensitivity linked to double-Intertropical Convergence Zone bias, Geophys. Res. Lett., 42(10), 4133–4141, doi:10.1002/2015GL064119, 2015.

Tian, B., Fetzer, E. J., Kahn, B. H., Teixeira, J., Manning, E. and Hearty, T.: Evaluating CMIP5 models using AIRS tropospheric air temperature and specific humidity climatology, J. Geophys. Res. Atmos., 118(1), 114–134, doi:10.1029/2012JD018607, 2013.

Tiedtke, M.: The sensitivity of the time-mean large-scale flow to cumulus convection in the ECMWF model. Proc. Work-shop on Convection in Large-Scale Models, Reading, United Kingdom, ECMWF, 297–316, 1983.

Waliser, D., Sperber, K., Hendon, H., Kim, D., Maloney, E., Wheeler, M., Weickmann, K., Zhang, C., Donner, L., Gottschalck, J., Higgins, W., Kang, I. S., Legler, D., Moncrieff, M., Schubert, S., Stern, W., Vitart, F., Wang, B., Wang, W. and Woolnough, S.: MJO simulation diagnostics, J. Clim., 22(11), 3006–3030, doi:10.1175/2008JCLI2731.1, 2009.

Wallace, J. M. and Gutzler, D. S.: Teleconnections in the Geopotential Height Field during the Northern Hemisphere Winter, Mon. Weather Rev., 109(4), 784–812, doi:10.1175/1520-0493(1981)109<0784:TITGHF>2.0.CO;2, 1981.

Wang, C., Zhang, L. and Lee, S.: A global perspective on CMIP5 climate model biases, Nat. Clim. Chang., 4(3), 201–205, doi:10.1038/NCLIMATE2118, 2014.

Wanner, H., Brönnimann, S., Casty, C., Luterbacher, J., Schmutz, C. and David, B.: North Atlantic Oscillation – Concepts and Studies, Surv. Geophys., 22(1984), 321–382, doi:10.1023/A:1014217317898, 2001.

Weaver, A. J., Sedláček, J., Eby, M., Alexander, K., Crespin, E., Fichefet, T., Philippon-Berthier, G., Joos, F., Kawamiy, M., Matsumoto, K., Steinacher, M., Tachiiri, K., Tokos, K., Yoshimori, M. and Zickfeld, K.: Stability of the Atlantic meridional overturning circulation: A model intercomparison, Geophys. Res. Lett., 39(20), 1–7, doi:10.1029/2012GL053763, 2012.

Winton, M.: A reformulated three-layer sea ice model, J. Atmos. Ocean. Technol., 17(4), 525–531, doi:10.1175/1520-0426(2000)017<0525:ARTLSI>2.0.CO;2, 2000.

Wu, X. and Mao, J.: Interdecadal variability of early summer monsoon rainfall over South China in association with the Pacific Decadal Oscillation, Int. J. Climatol., doi:10.1002/joc.4734, 2016.

Wu, Z., Li, J., Jiang, Z., He, J. and Zhu, X.: Possible effects of the North Atlantic Oscillation on the strengthening relationship between the East Asian Summer monsoon and ENSO, Int. J. Climatol., 32(5), 794–800, doi:10.1002/joc.2309, 2012.

Xie, S.-P.: A Dynamic Ocean – Atmosphere Model of the Tropical Atlantic Decadal Variability, J. Clim., 12(1), 64–71, 1999.

Xie, S. -P. and Philander, S. G. H.: A coupled ocean-atmosphere model of relevance to the ITCZ in the eastern Pacific, Tellus A, 46(4), 340–350, doi:10.1034/j.1600-0870.1994.t01-1-00001.x, 1994.

Xie, P., and P.A. Arkin, 1997: Global precipitation: A 17-year monthly analysis based on gauge observations, satellite estimates, and numerical model outputs. Bull. Amer. Meteor. Soc., 78, 2539 - 2558.

Xue, Y., Sellers, P., Kinter, J. and Shukla, J.: A Simplified Biosphere Model for Global

Climate Studies, J. Clim., 4(3), 345–364, doi:10.1175/1520-0442(1991)004<0345:ASBMFG>2.0.CO;2, 1991.

Yu, B. and Zwiers, F. W.: The impact of combined ENSO and PDO on the PNA climate: A 1,000-year climate modeling study, Clim. Dyn., 29(7–8), 837–851, doi:10.1007/s00382-007-0267-4, 2007.

Yu, R. and Zhou, T.: Impacts of winter-NAO on March cooling trends over subtropical Eurasia continent in the recent half century, Geophys. Res. Lett., 31(12), 3–6, doi:10.1029/2004GL019814, 2004.

Yuan, X. and Yonekura, E.: Decadal variability in the Southern Hemisphere, J. Geophys. Res, 116(D19), 1–12, doi:10.1029/2011JD015673, 2011.

Zebiak, S. E.: Air–Sea Interaction in the Equatorial Atlantic Region, J. Clim., 6(8), 1567–1586, doi:10.1175/1520-0442(1993)006<1567:AIITEA>2.0.CO;2, 1993.

Zhang, C.: Madden-Julian Oscillation, Rev. Geophys., 43(2), 1–36, doi:10.1029/2004RG000158, 2005.

Zhang, L. and Wang, C.: Multidecadal North Atlantic sea surface temperature and Atlantic meridional overturning circulation variability in CMIP5 historical simulations, J. Geophys. Res. Ocean., 118(10), 5772–5791, doi:10.1002/jgrc.20390, 2013.

Zhang, L., Ma, H. and Wu, L.: Dynamics and mechanisms of decadal variability of the Pacific-South America mode over the 20th century, Clim. Dyn., 46(11–12), 3657–3667, doi:10.1007/s00382-015-2794-8, 2016.

Zheng, F., Li, J., Clark, R. T. and Nnamchi, H. C.: Simulation and projection of the Southern Hemisphere annular mode in CMIP5 models, J. Clim., 26(24), 9860–9879, doi:10.1175/JCLI-D-13-00204.1, 2013.

1   **List of Figures**
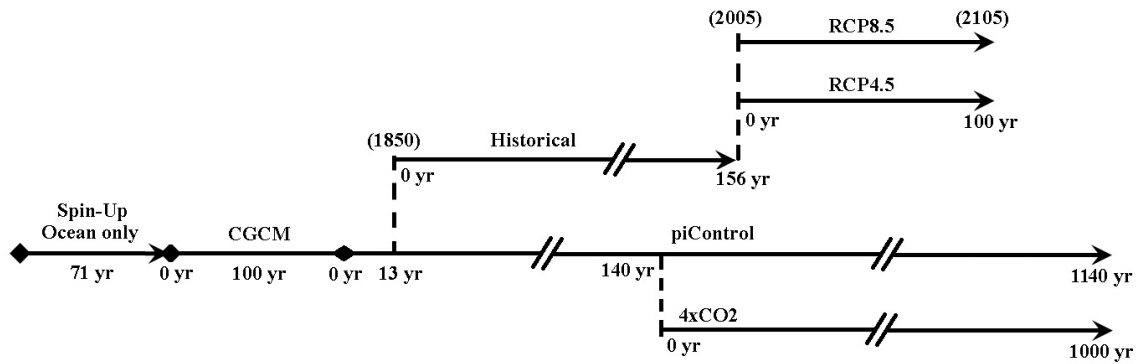
4   Figure 1 – The scheme of principal simulations carried out by BESM-OA2.5 using

5   different forcing conditions according to CMIP5 protocols. The date for the Historical

6   and RCPs simulations are from actual calendar years.
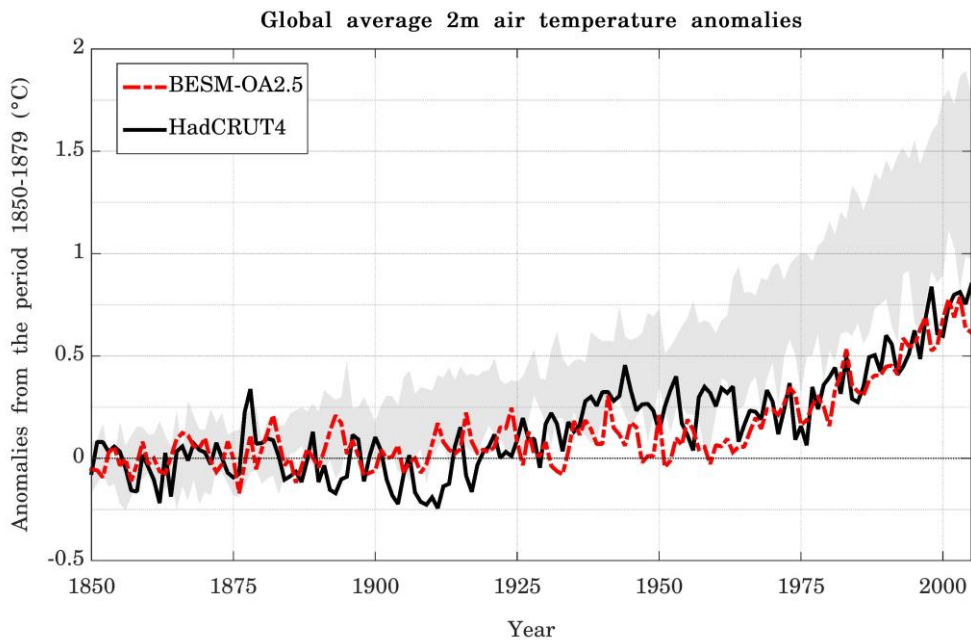
3 Figure 2 – Global averaged 2-m annual mean air temperature anomalies relative to the

4 period 1850–1879 for BESM-OA2.5 (dashed red line) and observation (solid black

5 line). The grey shadow represents the spread of 11 CMIP5 models (historical GHG

6 simulations). The CMIP5 models anomalies are also computed relative to the period

7 1850–1879, with exception of GFDL-ESM2M and HadGEM2-ES which anomalies are

8 computed relative to the periods 1861−1890 and 1860−1889, respectively. Units are in

9 ℃.
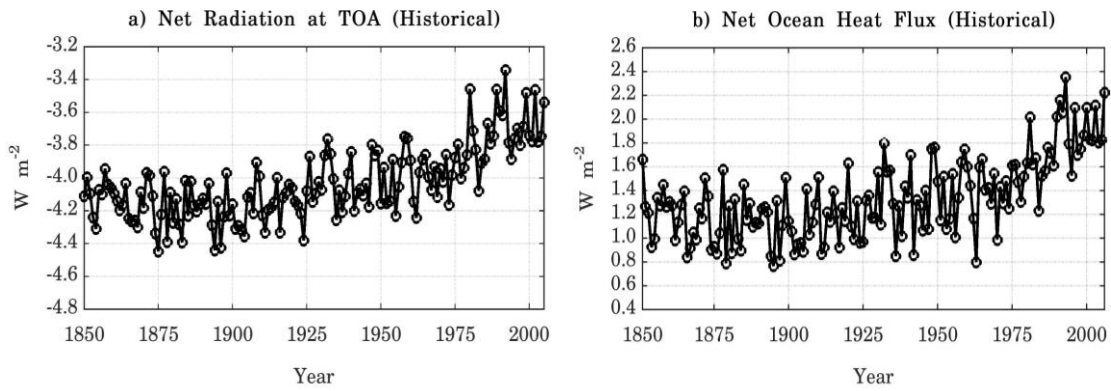
2 Figure 3 – Annual average time series for the global average (a) net of the radiation at

3 TOA (positive values indicates that the atmosphere is warming) and (b) net of the

4 ocean/atmosphere heat flux (positive values indicates that the ocean is warming),

5 simulated by the Historical run over the period 1850-2005 (156 years).

a) Annual mean precipitation (BESM-OA2.5)
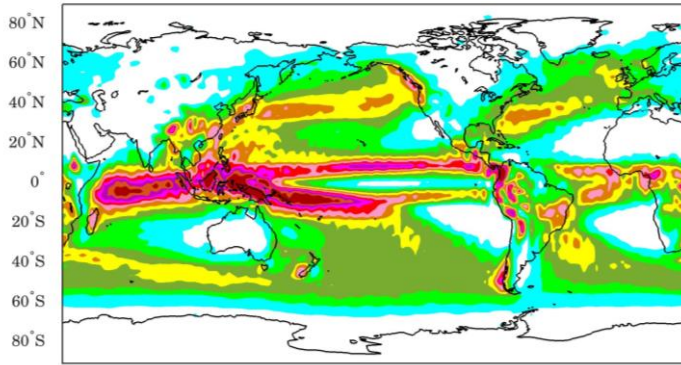
b) Annual mean precipitation (GPCP)
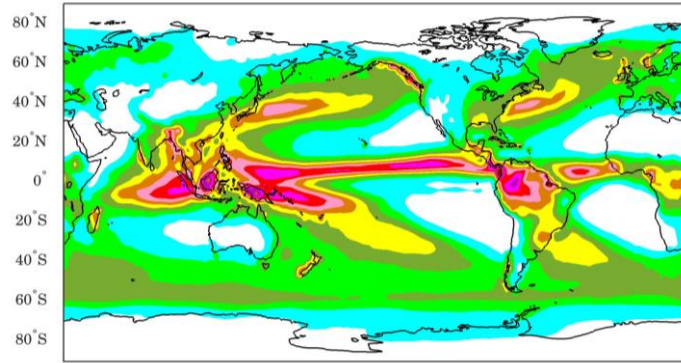
c) BESM-OA2.5 - GPCP   mean: 0.3 mm/day   rmse: 1.4 mm/day
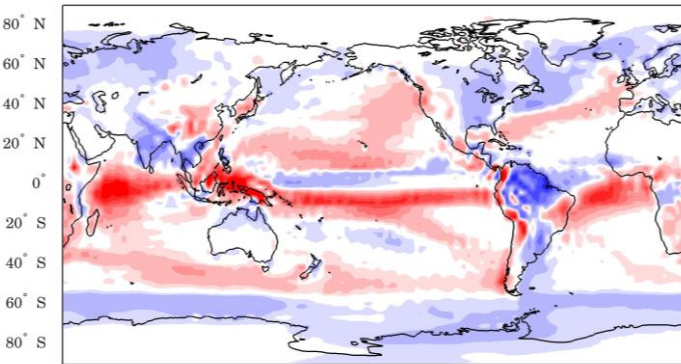
d) BESM-OA2.5 - CMAP   mean: 0.4 mm/day   rmse: 1.5 mm/day
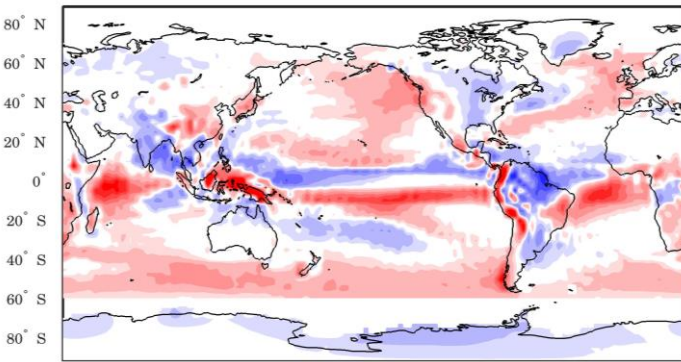
1   Figure 4 – Spatial map of annual mean precipitation for (a) BESM-OA2.5, for (b)

2   GPCP, (c) the bias of BESM-OA2.5 relative to GPCP and (d) the bias of BESM-OA2.5

3   relative to CMAP. The averages values are computed over the periods 1971–2000 (for

4   BESM-OA2.5) and 1979–2008 (for GPCP and CMAP). Units are in mm day^{-1}.

a) BESM-OA2.5 200 hPa Vel. Potential/Div. Wind
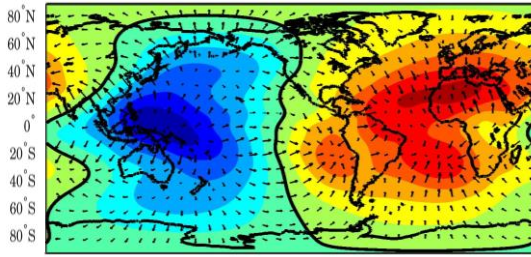
b) 20CRv2 200 hPa Vel. Potential/Div. Wind
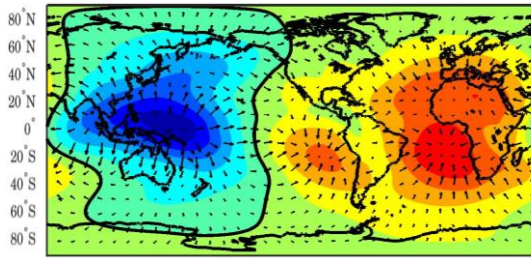
c) BESM-OA2.5 Bias 200 hPa Vel. Potential/Div. Wind
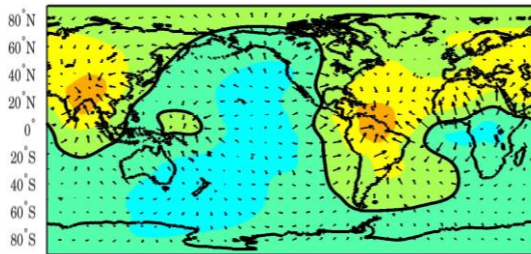
d) BESM-OA2.5 Bias 200 hPa Vel. Potential/Div. Wind MAM
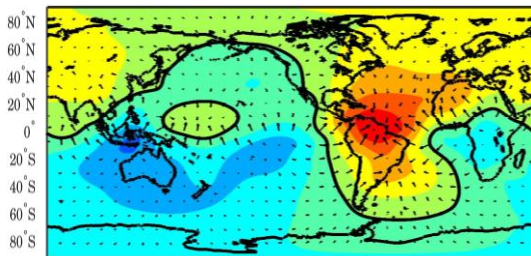
e) BESM-OA2.5 Bias 200 hPa Vel. Potential/Div. Wind JJA

-1.2 -1.0 -0.8 -0.6 -0.4 -0.2 0 0.2 0.4 0.6 0.8 1.0 1.2

$m^2 \ s^{-1}$
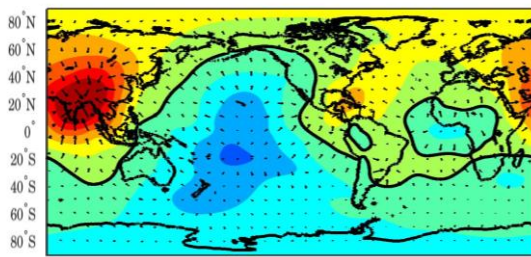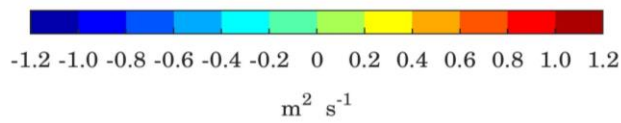
1 Figure 5 – Spatial maps with averaged global anomalies of velocity potential and wind

2 divergence at 200 hPa pressure level for (a) BESM-OA2.5 and (b) Reanalysis. (c) The

3 bias of the model relative to the Reanalysis, (d) and (e) are the bias for MAM and JJA

4 seasons, respectively. The averages are computed over the period 1950–2005. Units are

5 in m s^{-1}.
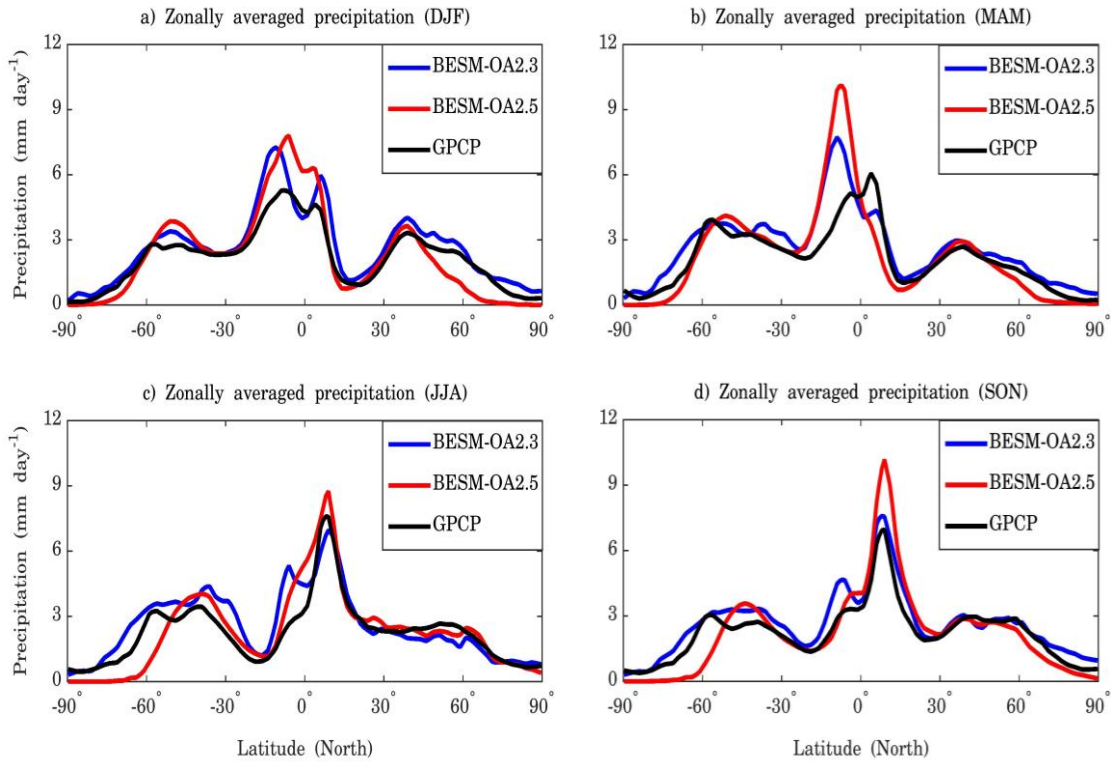
Figure 6 – Zonally averaged annual mean precipitation for BESM-OA2.5, BESM-OA2.3 and GPCP dataset relative to the seasons DJF, MAM, JJA and SON. The zonally averages values are computed over the periods 1971–2000 and 1979–2008, for BESM-OA2.5 and GPCP, respectively. Units are in mm day^{-1}.

a) Total cloud fraction (BESM-OA2.5 - ISCCP)
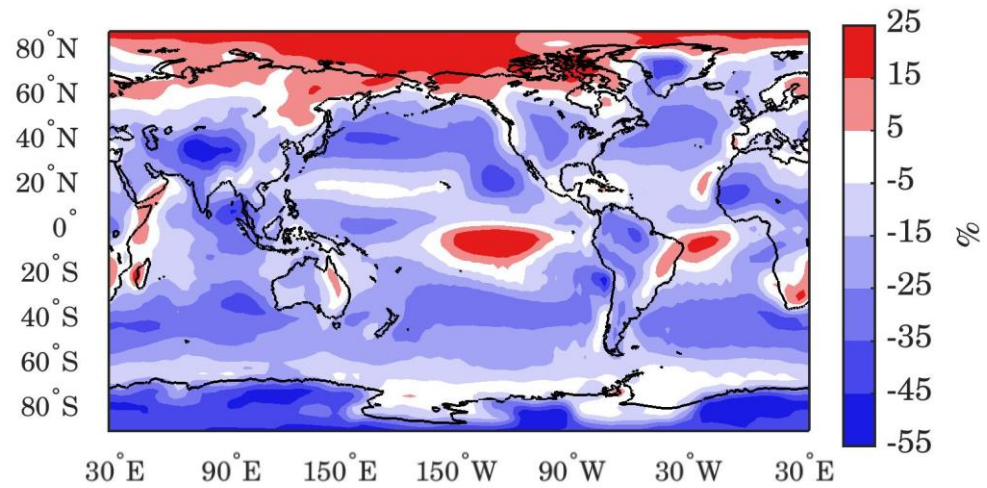
b) Zonally averaged total cloud cover
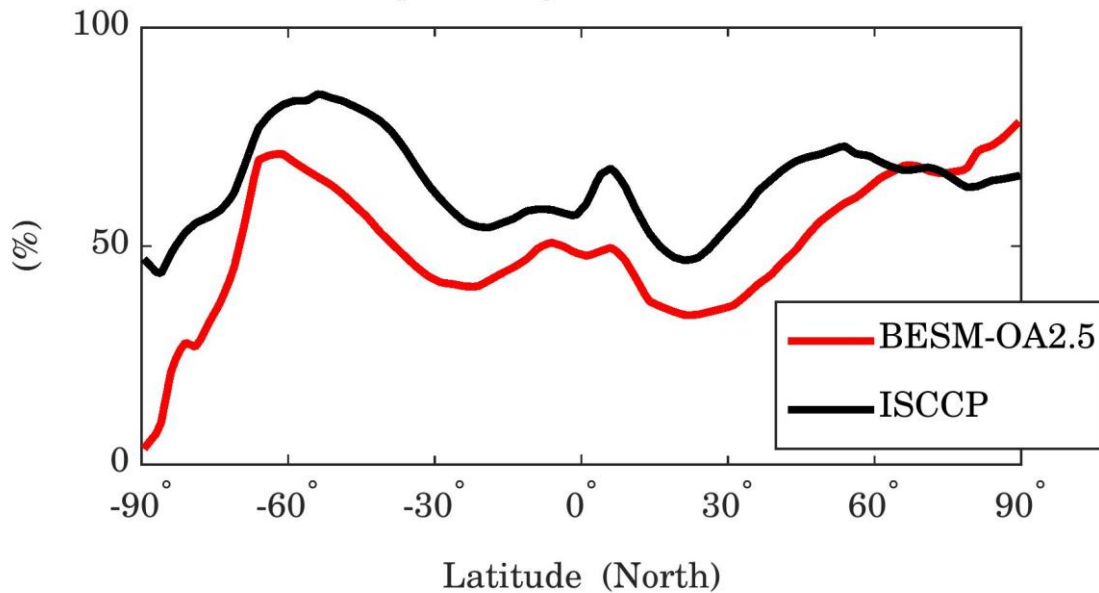
Figure 7 – (a) Spatial map of annual mean total cloud fraction bias of BESM-OA2.5

relative to ISCCP. (b) Zonally averaged total cloud cover for BESM-OA2.5 and ISCCP

dataset. The periods used are 1971–2000 and 1984–2009 for BESM-OA2.5 and ISCCP,

respectively. Units are in percentage.
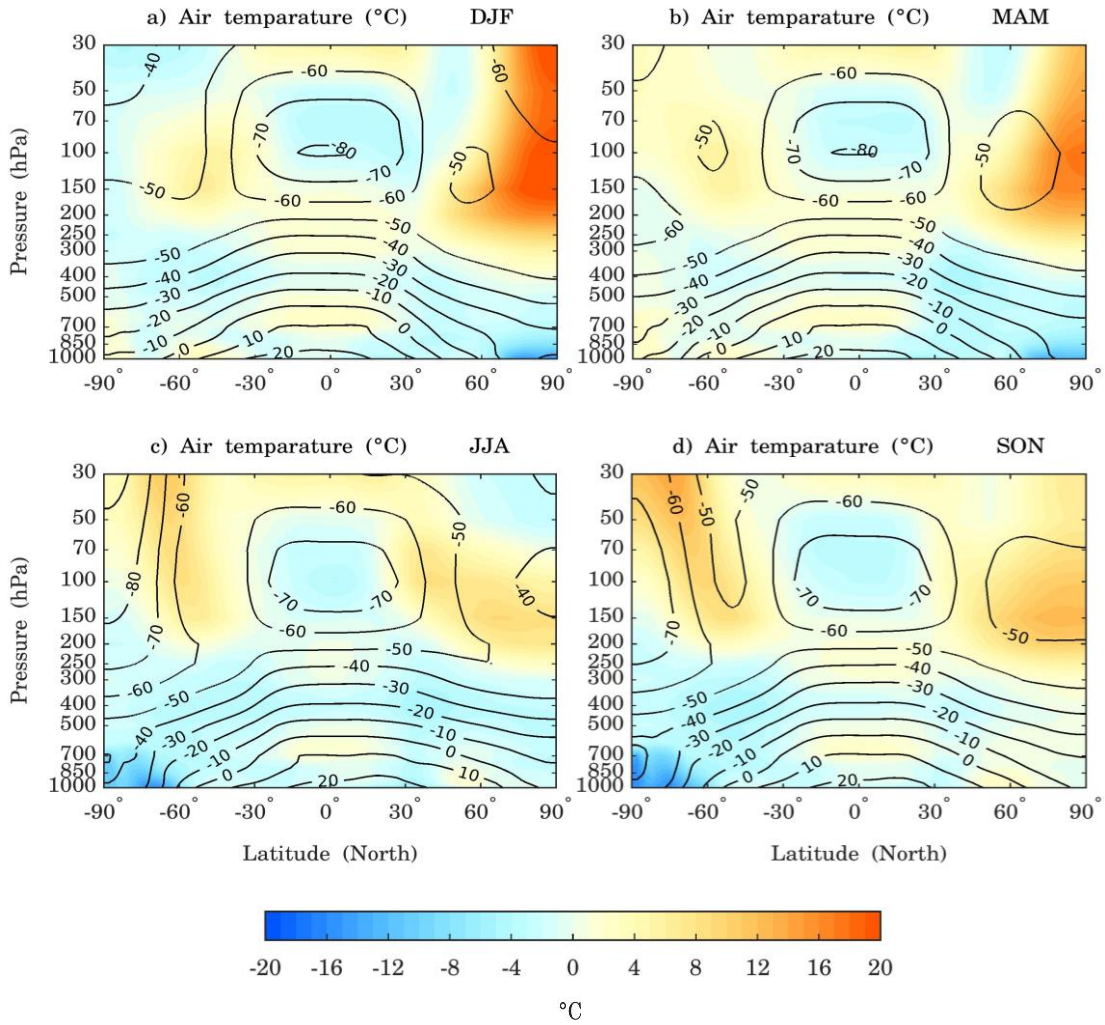
Figure 8 – Contour lines are the zonally averaged vertical air temperature for BESM-

OA2.5 and in shaded are the difference BESM-OA2.5 - 20CRv2 data set. Both are

averaged over the period 1971–2000. The units are in ℃ and the contour interval is 10

℃.
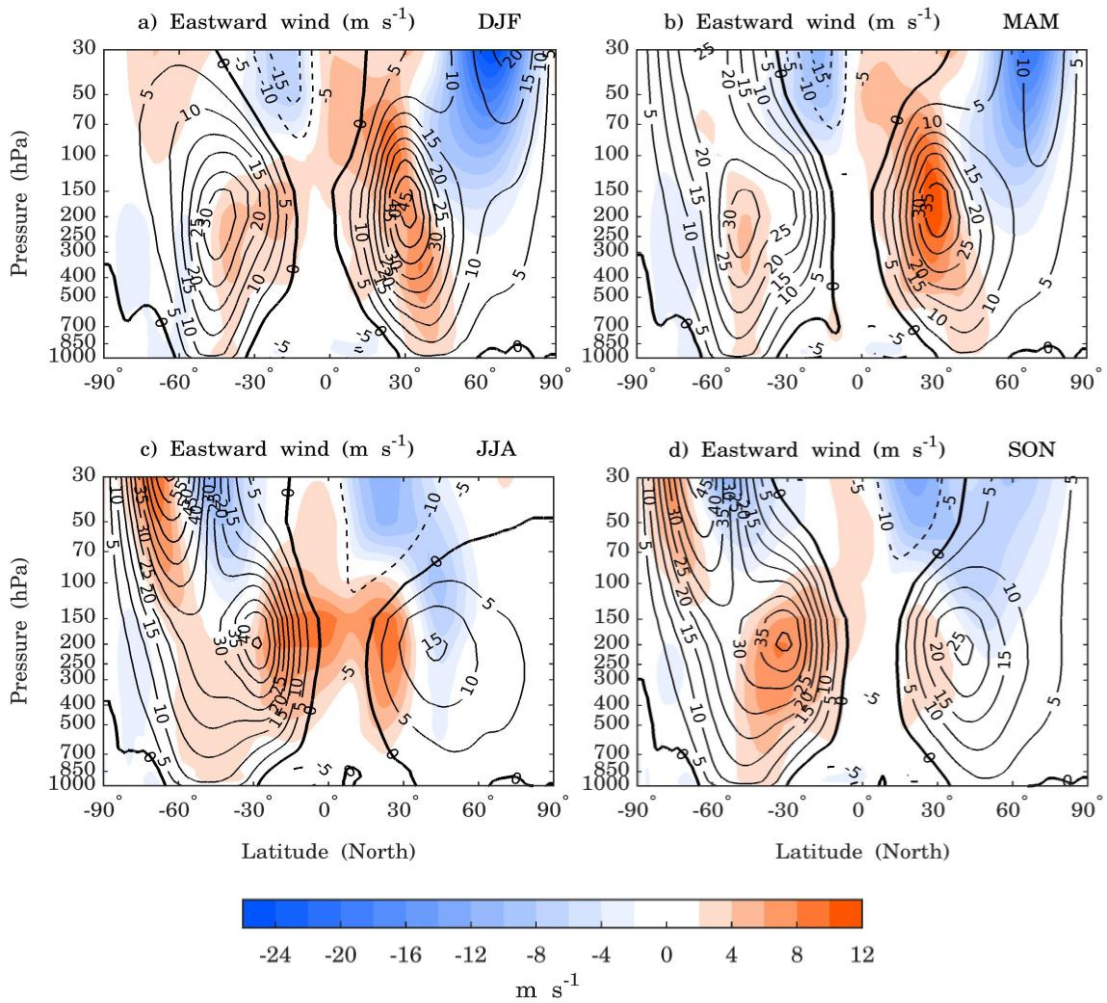
Figure 9 – Contour lines are the zonally averaged zonal wind for BESM-OA2.5 and in shaded are the difference BESM-OA2.5 - 20CRv2 data set. Both are averaged over the period 1971–2000. The solid contour lines represent eastward zonal wind and the dashed contour lines represents westward zonal wind. The units are in meters per second and the contour interval is 5 m s^{-1}, with the contour line zero highlighted.
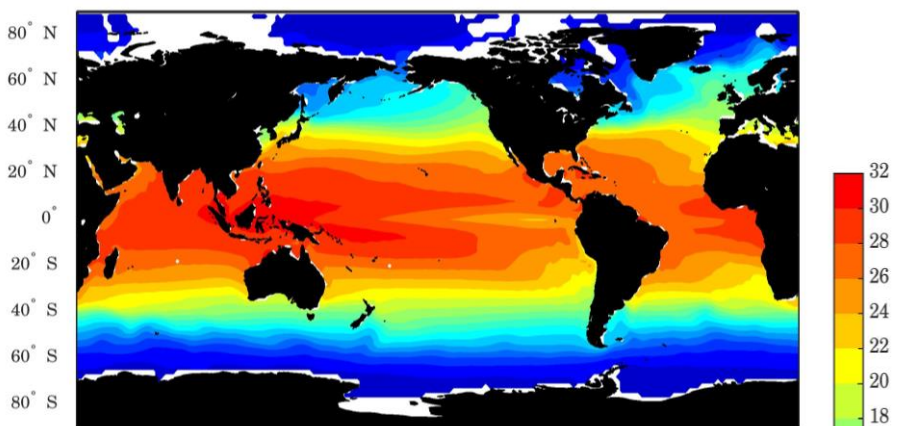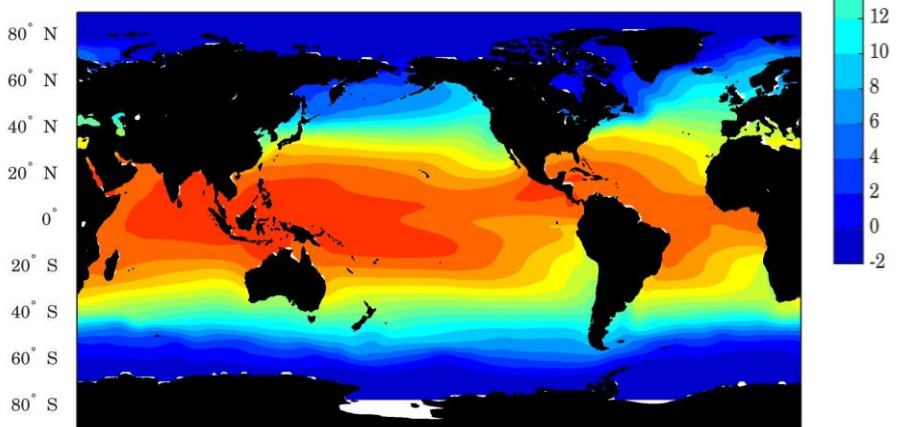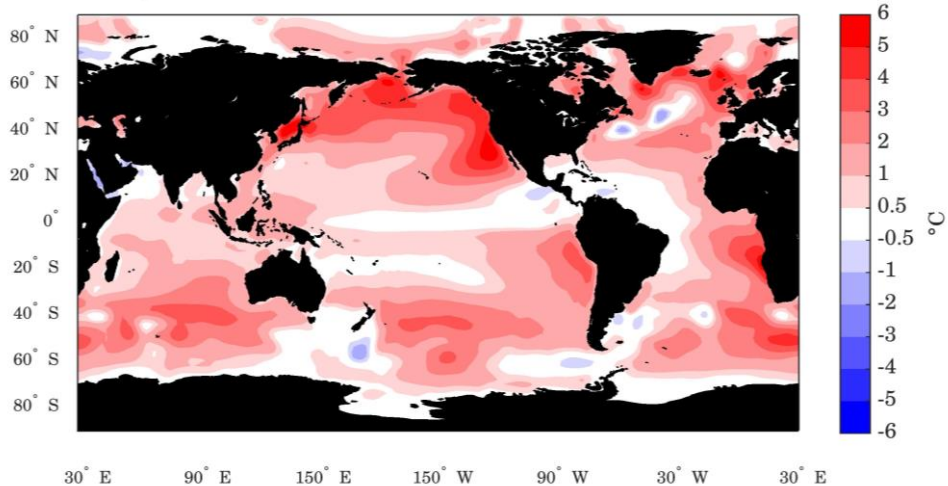
1   Figure 10 – Spatial map of annual mean sea surface temperature for (a) BESM-OA2.5,

2   (b) ERSSTv4 and (c) the bias of BESM-OA2.5 relative to ERSSTv4. The averages are

3   computed over the period 1971–2000. Units are in °C.

a) Equatorial Pacific Mean SST
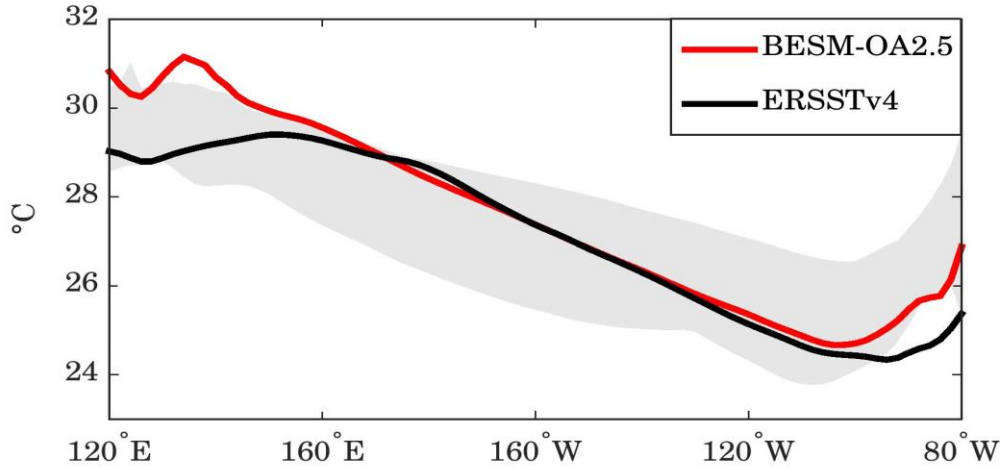
b) BESM-OA2.5
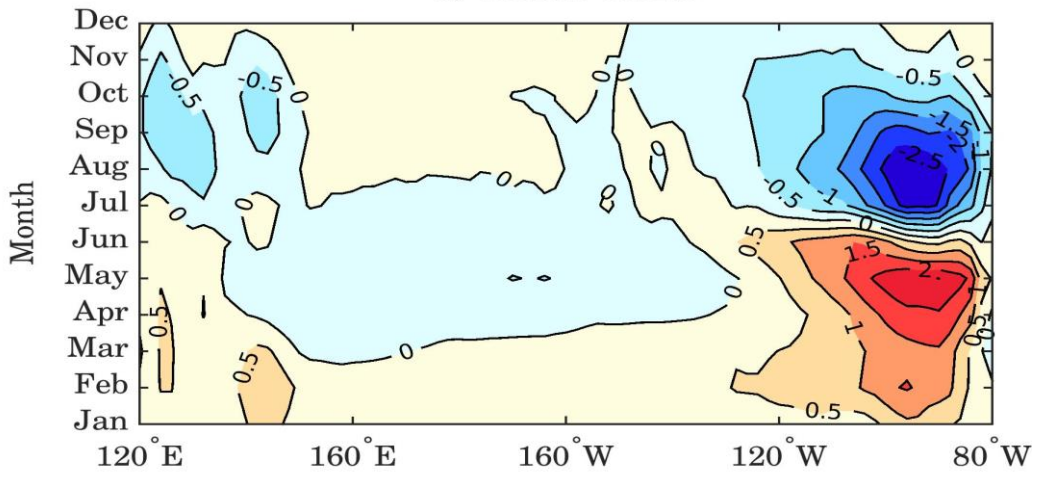
c) ERSSTv4
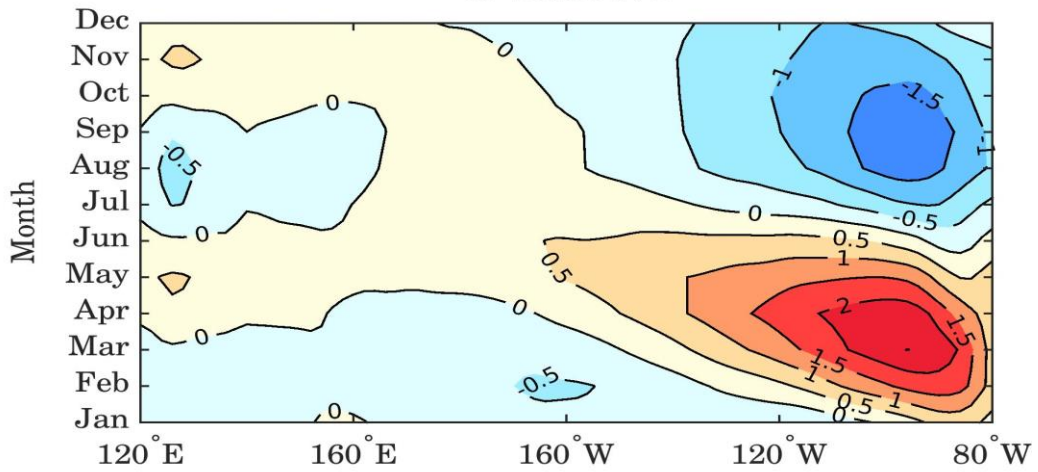
1 Figure 11 – (a) Mean SST along the equator in the Pacific Ocean and annual cycle of

2 the equatorial Pacific SST anomalies for (b) BESM-OA2.5 and (c) ERSSTv4.

3 Equatorial region is defined by averaging over 2 °S–2 °N. BESM-OA2.5 and ERSSTv4

4 are averaged over the period 1971–2000. In (a) the grey shadow represents the spread of

5 11 CMIP5 models, which are also averaged over the period 1971–2000. Units are in ℃.
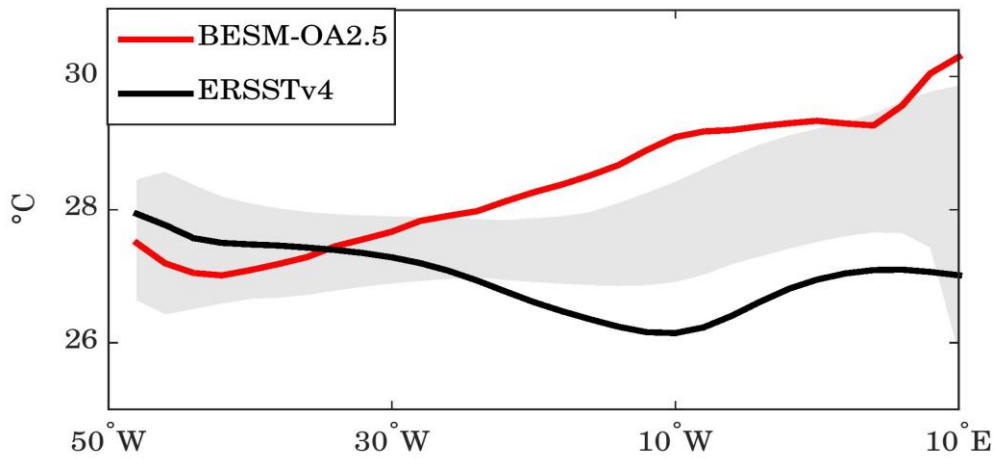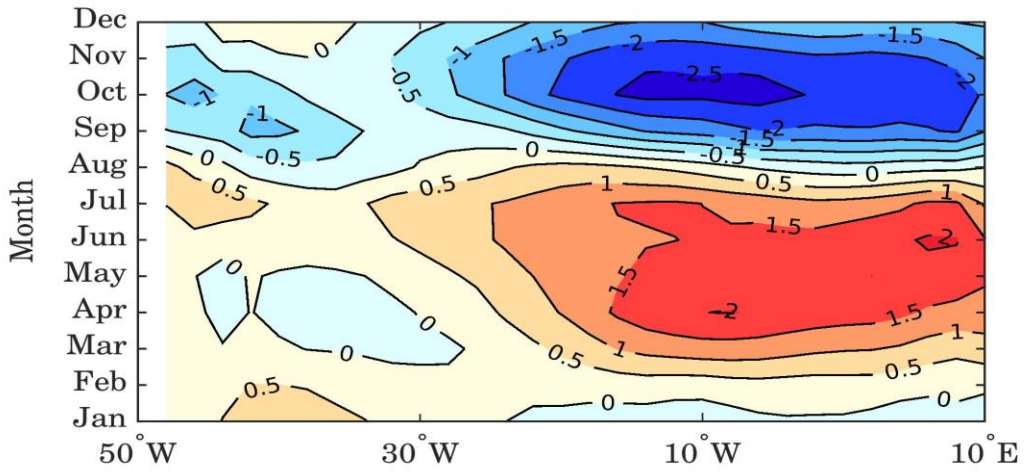
Figure 12 – As Fig. 11 but for the Atlantic Ocean.

a) Ocean Salinity Anomaly from IC (Historical)

b) Ocean Temperaure Anomaly from IC (Historical)

c) Ocean Temperaure Anomaly from IC (piControl)

d) Ocean Temp. Anom. (Historical - piControl)
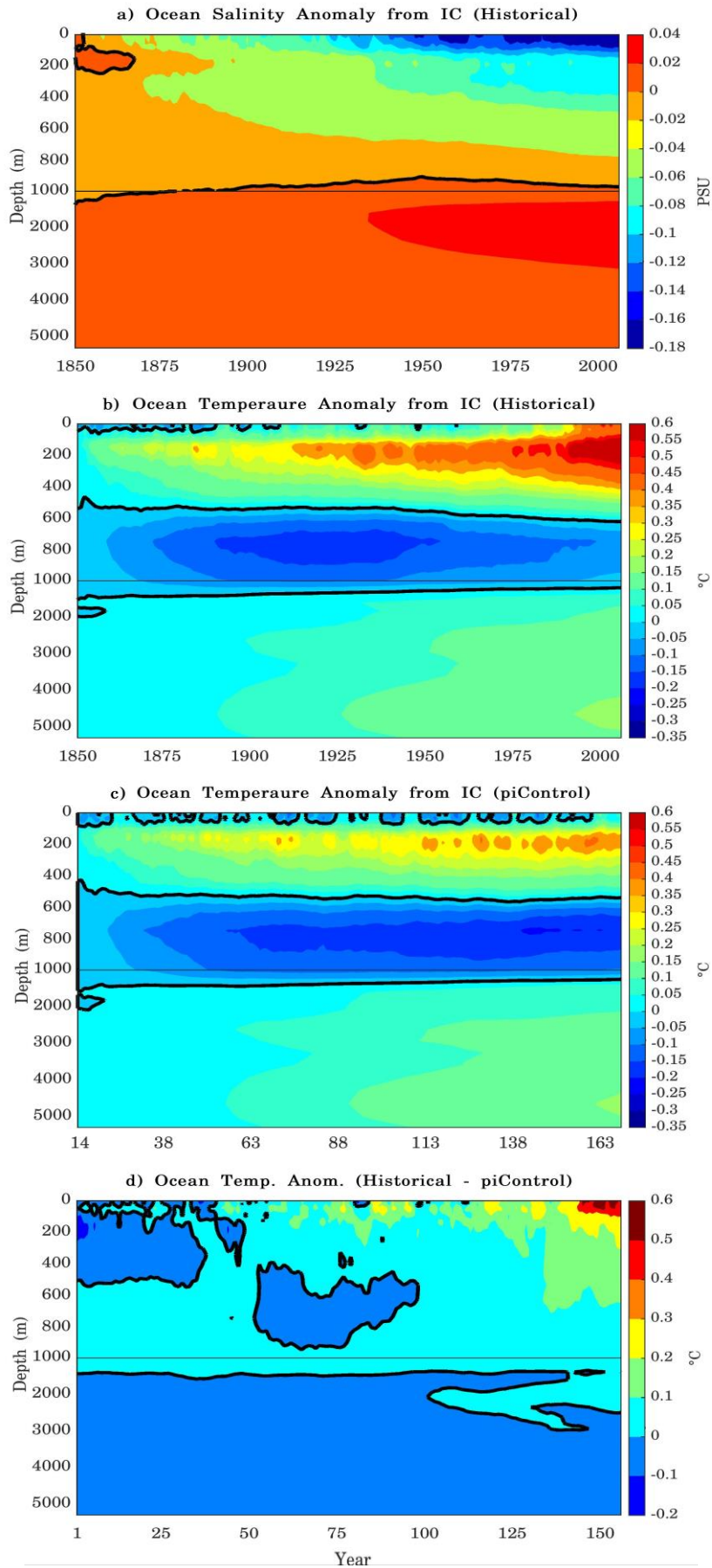
1   Figure 13 – Depth-time Hovmöller diagrams of global average ocean (a)salinity and (b)

2   temperature anomalies from the respective initial conditions (IC). Here the initial

3   conditions are taken from the 1th year for (a, b) Historical simulation, and 14th year for

4   (c) piControl simulation. (d) presents the difference between the temperature anomalies

5   of Historical relative to piControl. The diagrams are based on annual average time series

6   simulated by the Historical simulation over the period 1850-2005 (156 years) and by

7   piControl simulation over the period 14-169 years (156 years). The thick black line

8   represents the zero contours. Note that the vertical scales are different above and below

9   1000 m.
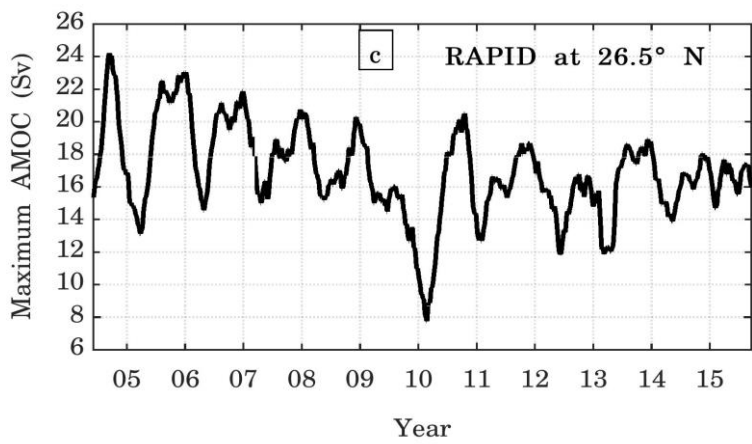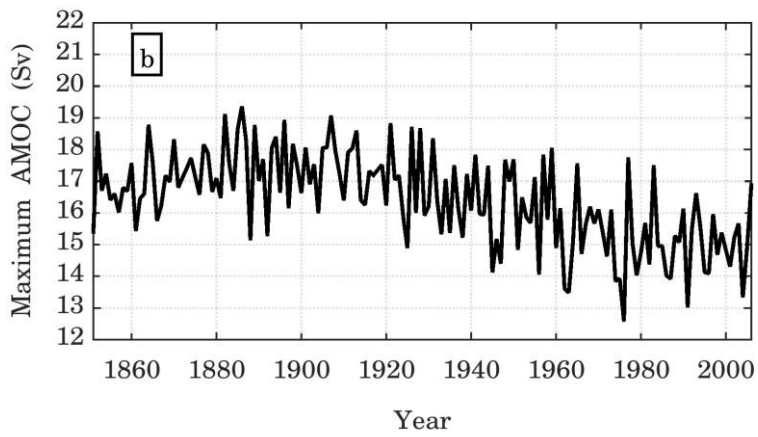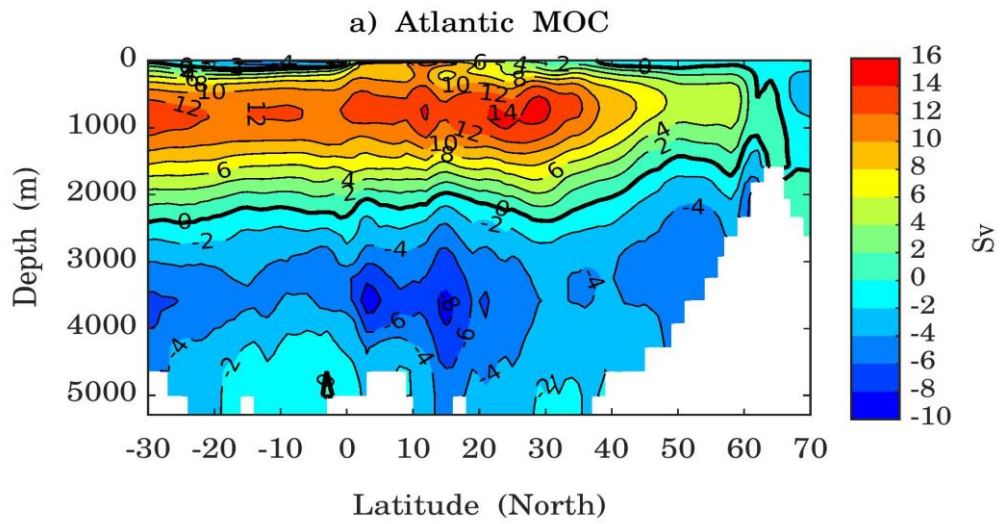
a) Atlantic MOC

1 Figure 14 – (a) Atlantic Meridional Overturning Circulation averaged for the period

2 1971–2000 and (b) annual mean maximum AMOC strength time series at the latitude

3 30 ºN simulated by BESM-OA2.5 for historical simulation over the period 1850–2005.

4 The smaller graph shows the AMOC time series measured by the project RAPID at

5 26.5 º N over the period April/2004 to October/2015. The RAPID time series is

6 smoothed by a 3-month running average. Units are in Sverdrup.
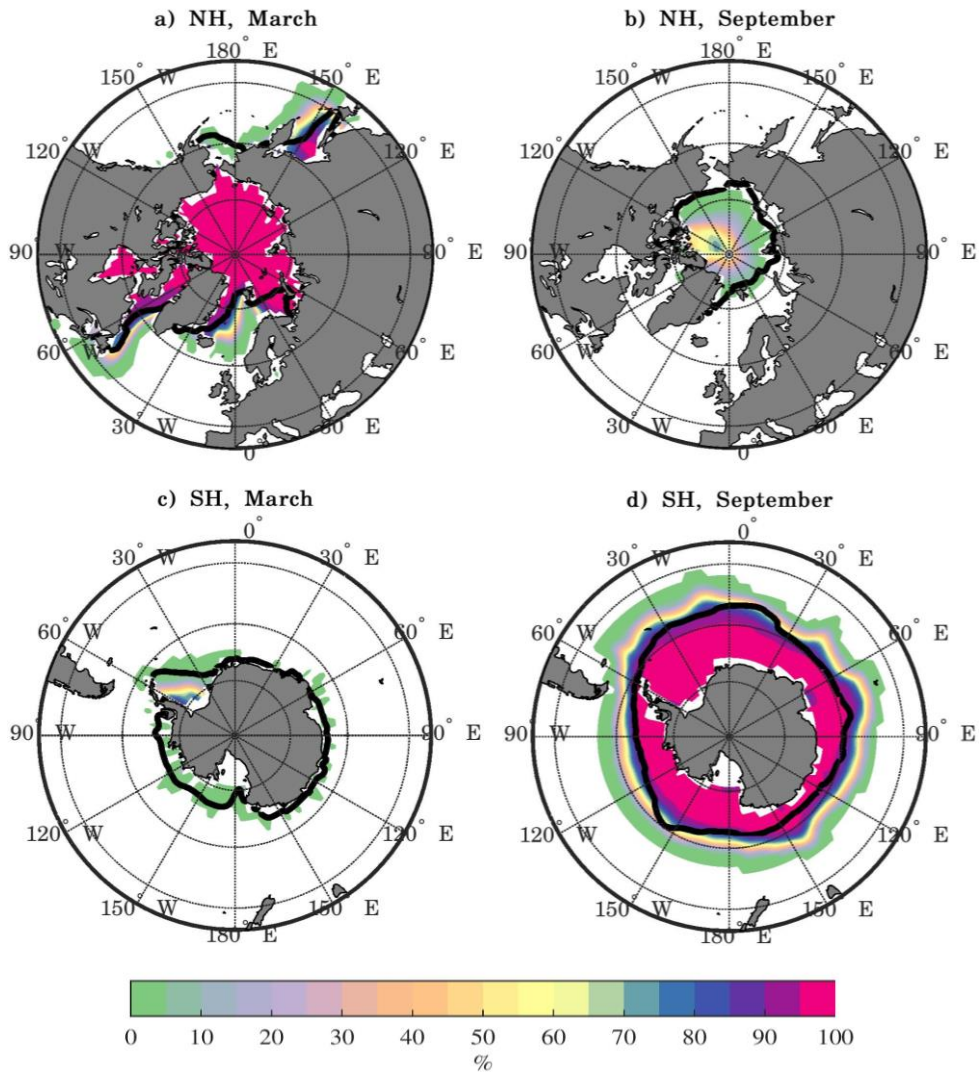
Figure 15 - BESM-OA2.5 mean sea ice concentration for March (a, c) and September (b, d) for each hemisphere. The solid black lines show the 15 % mean sea ice concentration for 20CRv2 Reanalysis. The averages values are computed over the period 1971–2000 for BESM-OA2.5 and 20CRv2. The concentration is presented in percentage.

a) Pacific SST EOF1 (17.9%) BESM-OA2.5
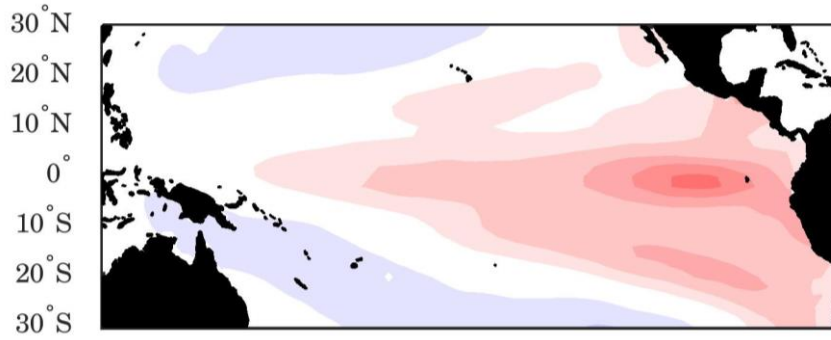
b) Pacific SST EOF1 (45.0%) ERSSTv4
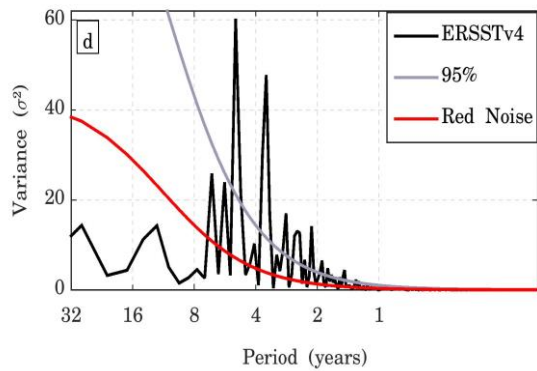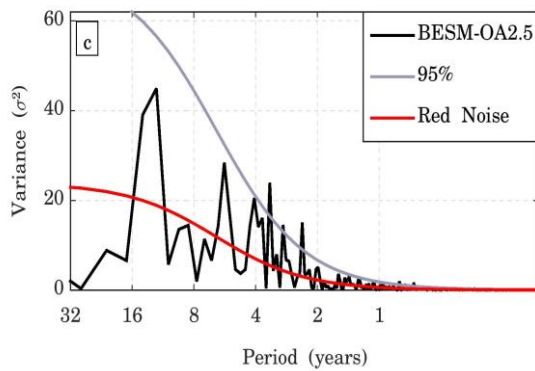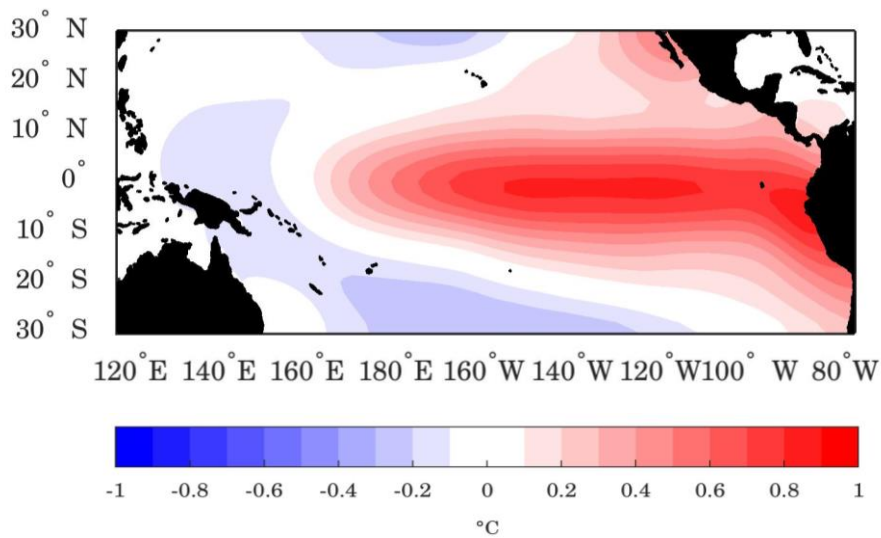
Figure 16 – The leading EOF modes of the detrended monthly SST anomalies over the

Tropical Pacific region (30 ° S–30 ° N; 240 °–70 ° W) for (a) BESM-OA2.5 and (b)

1   ERSSTv4. The results are shown as the SST anomalies regressed onto the

2   corresponding normalized PC time series (℃ per standard deviation) over the period

3   1950–2005. The percentage of the variance explained by each EOF is indicated in the

4   title of the figure. The contour interval is 0.1 ℃. Figures (c) and (d) are the power

5   spectrum of the leading joint PC time series of the pattern for BESM-OA2.5 and

6   ERSSTv4, respectively. The solid red line represents the theoretical red noise spectrum

7   and the gray line represents the 95 % confidence level.
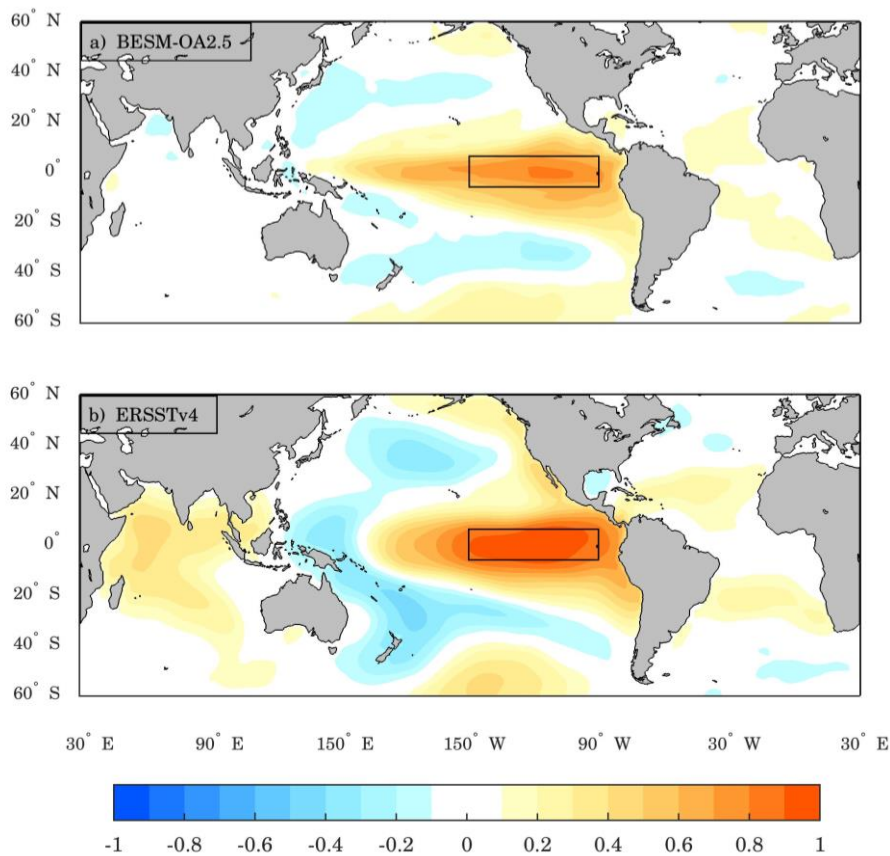
Figure 17 – Spatial maps with the monthly correlation between Ni ño-3 index and global SST anomalies computed for (a) BESM-OA2.5 and (b) ERSSTv4 over the period 1900–2005. The anomalies are obtained by subtracting the monthly means for the whole detrended time series at each grid point. Black rectangles show the Ni ño-3 index region. Shaded areas are statistically significant at the 95 % confidence level (through two tailed t-student test).

a) AMM jEOF1 (10.7%) BESM-OA2.5
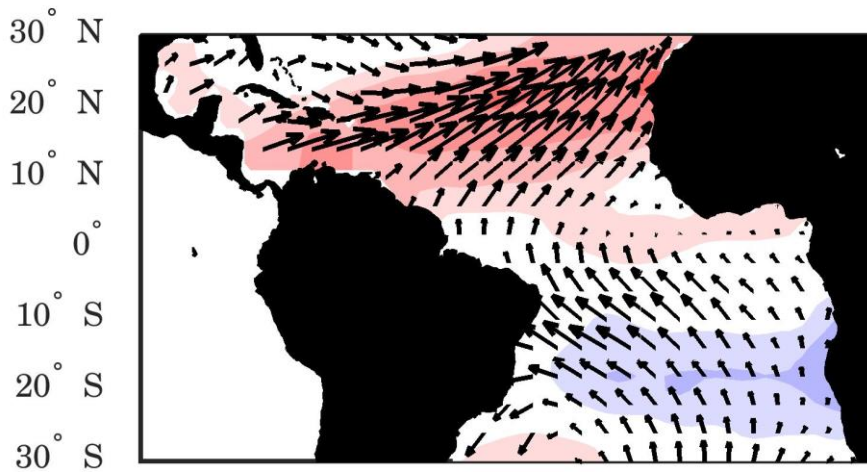
b) AMM jEOF1 (11.8%) ERSSTv4 (SST), 20CRv2 (Taux,Tauy)
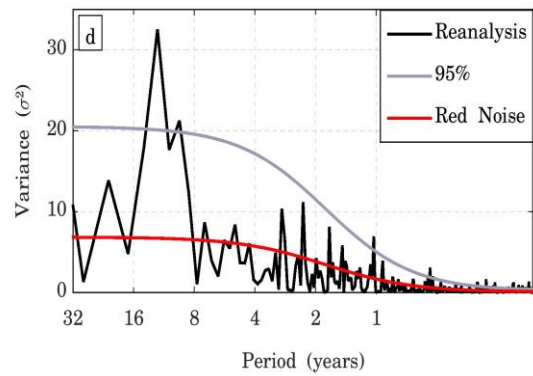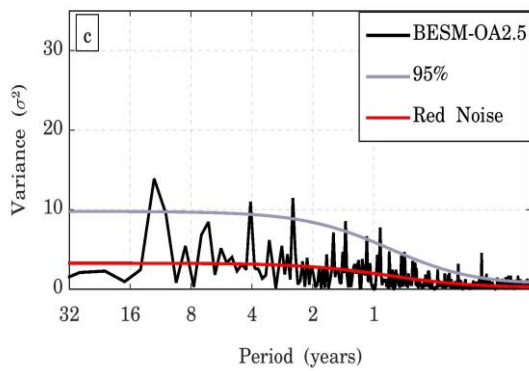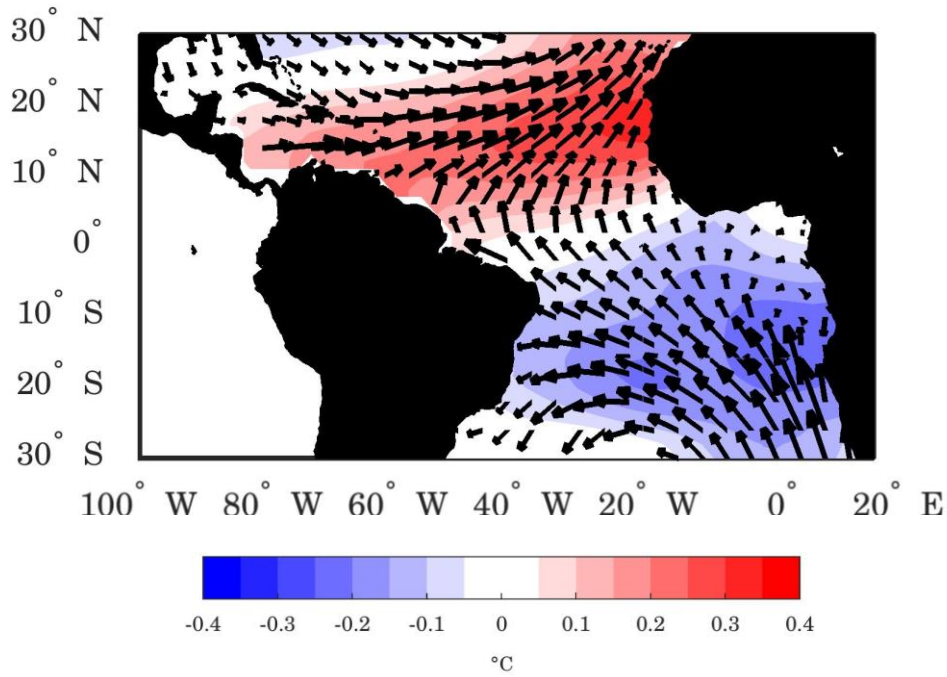
Figure 18 – The leading joint EOF modes of the detrended monthly SST and wind stress (Taux and Tauy) anomalies for the Tropical Atlantic region (30 °S–30 °N; 100 °W–20 ° E) for (a) BESM-OA2.5 and (b) for observation (ERSSTv4 and 20CRv2 Reanalysis). The results are shown as the SST anomalies regressed onto the corresponding normalized PC time series (°C per standard deviation) and wind stress anomalies regressed onto the corresponding normalized PC time series (ms^{-1} per standard deviation) over the period 1950–2005. The percentage of the variance explained by each EOF is indicated in the title of the figure. The contour interval is 0.05 °C. Figures (c) and (d) are the power spectrum of the leading joint PC time series of the AMM pattern for BESM-OA2.5 and observation, respectively. The solid red line represents the theoretical red noise spectrum and the gray line represents the 95 % confidence level.
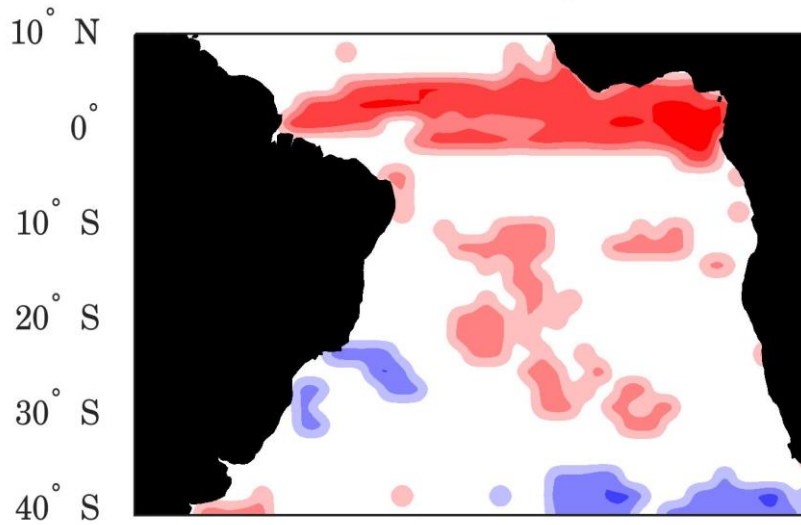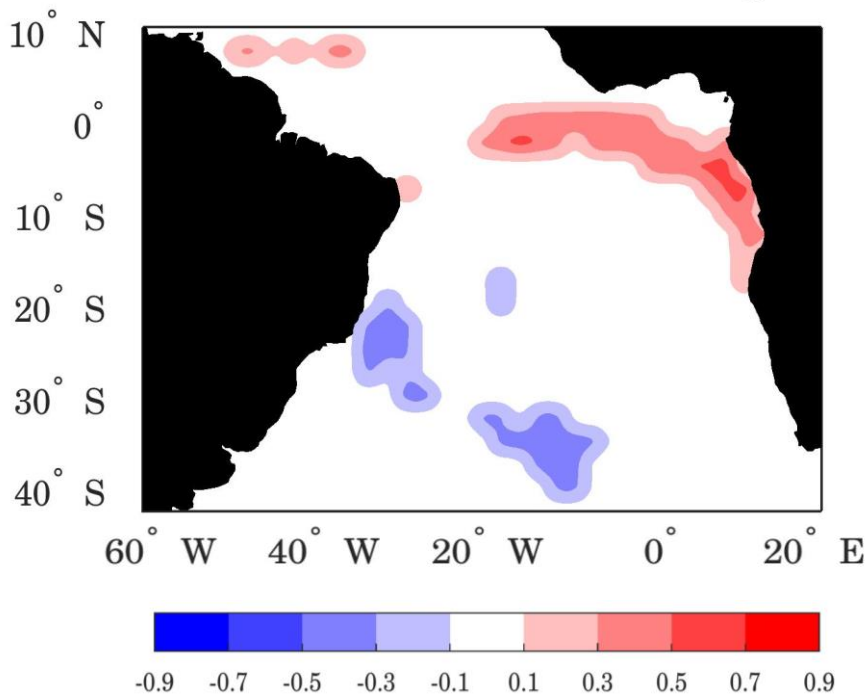
Figure 19 – Spatial maps with the correlation between SST and precipitation (seasonal average DJF) over the South Ocean (40º S−10º N; 70º W−20º E) computed for (a) BESM-OA2.5 over the period 1971−2002 and (b) observations over the period

1   1979−2010. Shaded areas are statistically significant at the 95 % confidence level

2   (through two tailed t-student test).
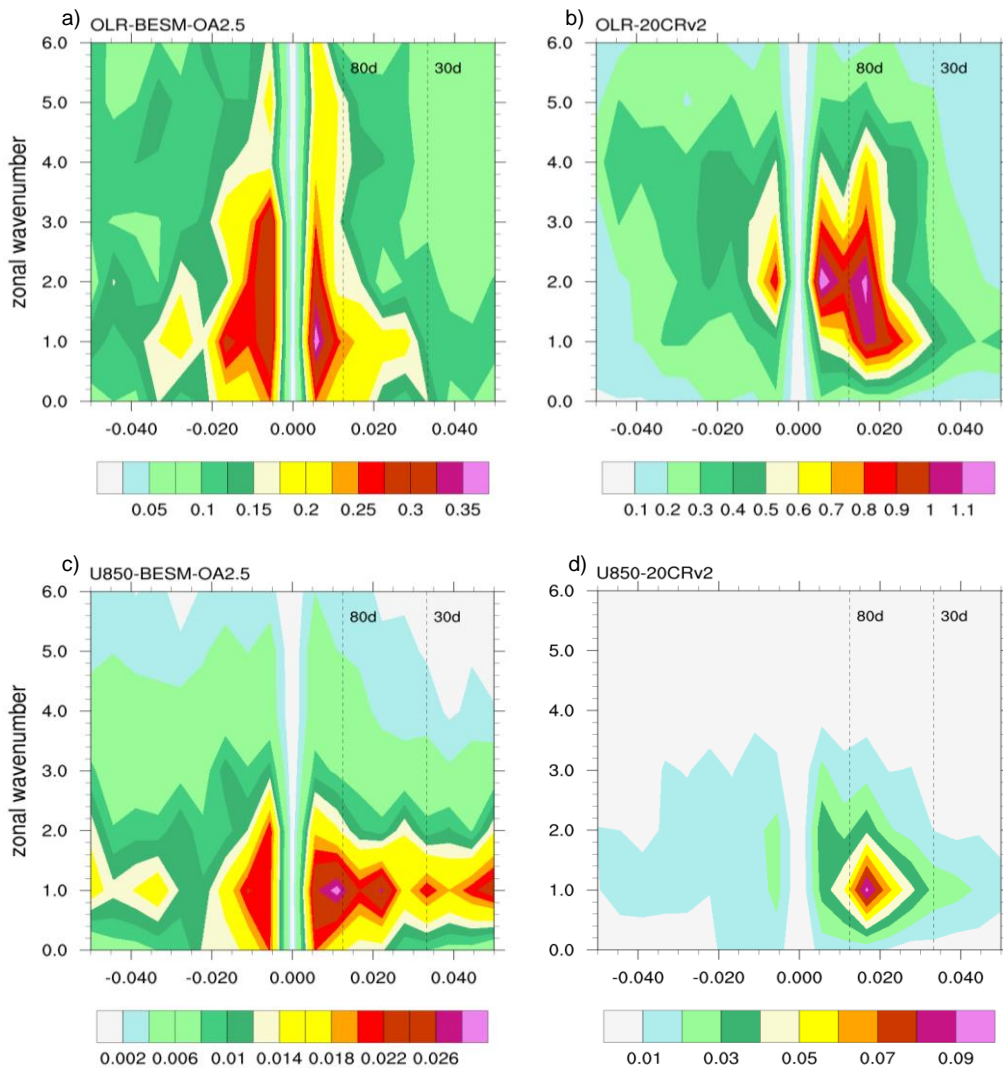
Figure 20 – Wavenumber-frequency power spectrum of tropical (10 ̊S–10 ̊N) averaged daily outgoing long-wave radiation (OLR) for (a) BESM-OA2.5 and (b) 20CRv2, respectively, and averaged daily zonal wind component at 850 hPa pressure level (U850) for (c) BESM-OA2.5 and (d) 20CRv2, respectively. Data used are daily anomalies for the boreal winter (Nov-Apr) over the period 1971–2000. Daily anomalies are obtained by subtracting the climatological daily mean calculated over the period 1971–2000. Individual spectra were calculated for each boreal winter and then averaged

1   over the time period used. Units for the zonal wind (OLR) are m^{-2} s^{-2} (W m^2 s^{-1}) per

2   frequency interval per wavenumber interval.
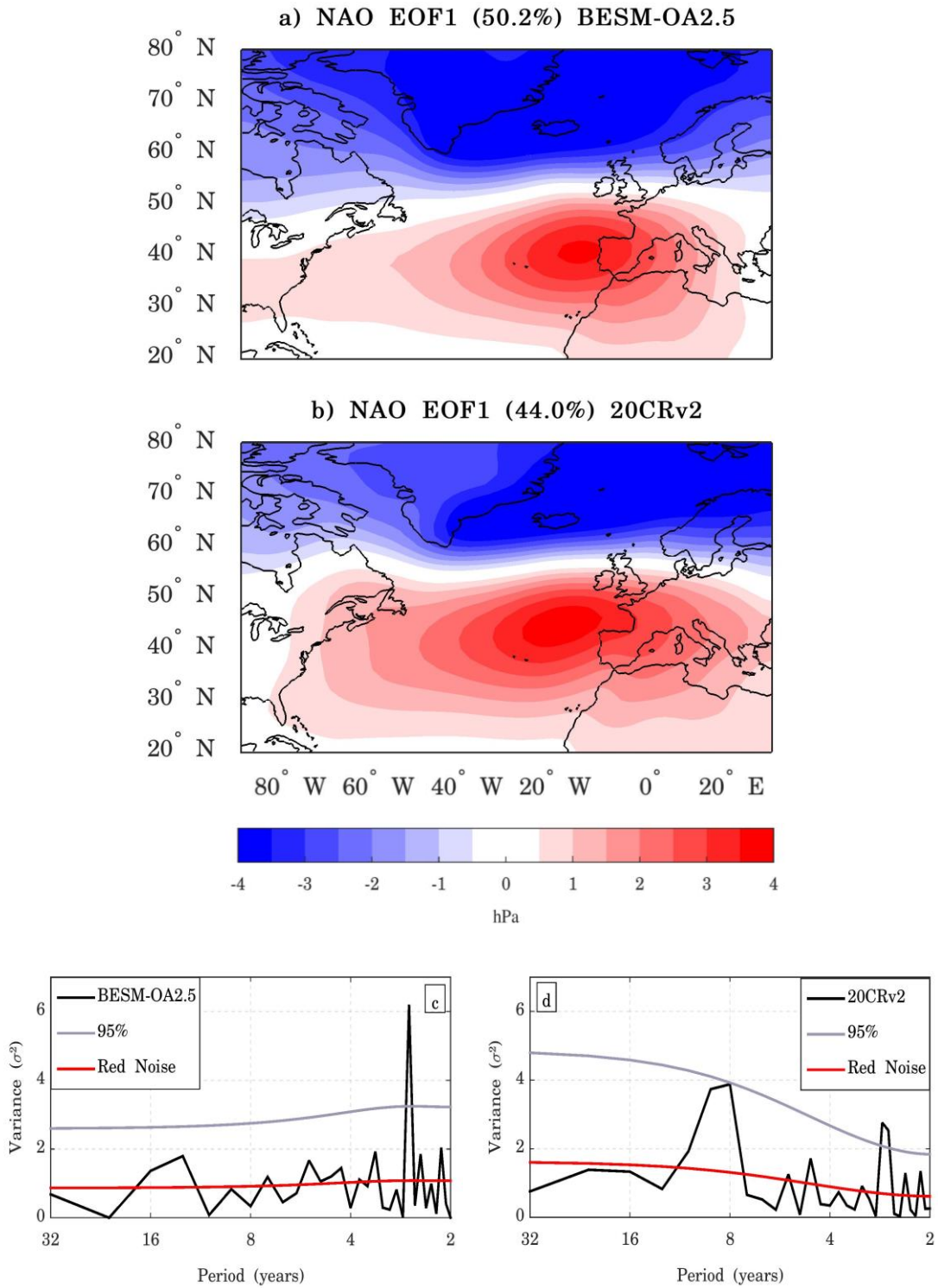
3   Figure 21 – The leading EOF modes of the boreal winter (DJF) seasonal averaged SLP

4   anomalies for the Euro-Atlantic region (20º−80º N; 100º W−30º E) for (a) BESM-

1   OA2.5 and (b) 20CRv2. The results are shown as the SLP anomalies regressed onto the

2   corresponding normalized PC time series (hPa per standard deviation) for the period

3   1950−2005. The percentage of the variance explained by each EOF is indicated at the

4   title of the figure. The contour interval is 0.5 hPa. Figures (c) and (d) are the power

5   spectrum of the leading PC time series of the NAO pattern for BESM-OA2.5 and

6   20CRv2, respectively. The solid red line represents the theoretical red noise spectrum

7   and the gray line represents the 95 % confidence level.
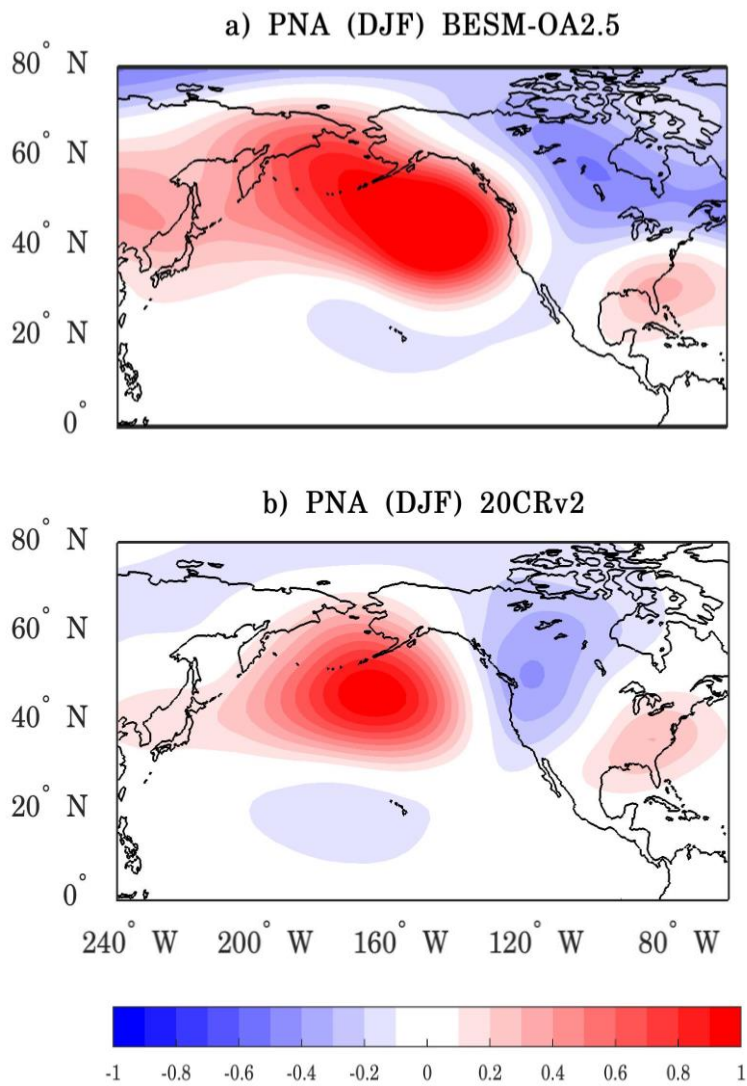
Figure 22 – One-point correlation map for (a) BESM-OA2.5 and (b) 20CRv2

Reanalysis showing the correlation coefficient of 500 hPa geopotential level based at

45 ºN, 165 ºW and the other grid points. The time series used are boreal winter seasonal

(DJF) averaged dataset for the period 1950−2005.
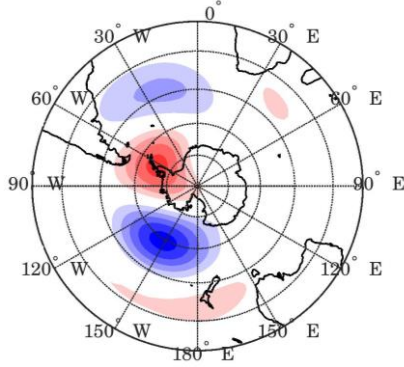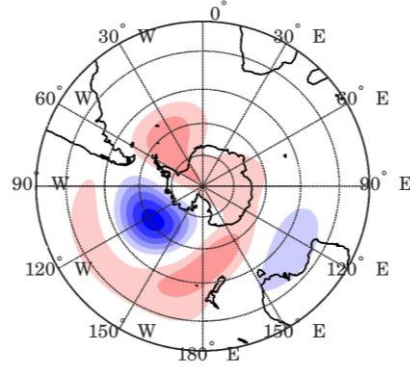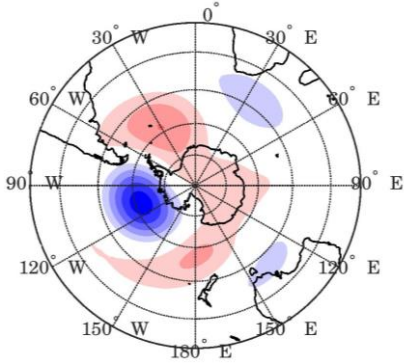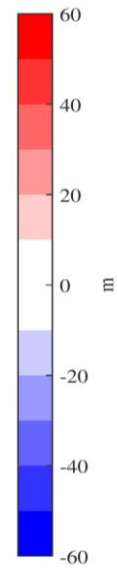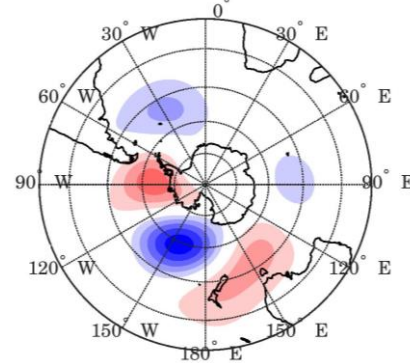
3   Figure 23 – (a) The second and third EOF modes of the monthly mean 500 hPa

4   geopotential height field for the Southern Hemisphere (20º−90º S) for BESM-OA2.5 (b)

5   and for 20CRv2 Reanalysis. The results are shown as the 500 hPa geopotential height

6   regressed onto the corresponding normalized PC time series (meters per standard

7   deviation) over the period 1950−2005. The percentage of the variance explained by

8   each EOF is indicated at the title of the figure. The contour interval is 10 m.

a) SAM EOF1 (34.1%) BESM-OA2.5
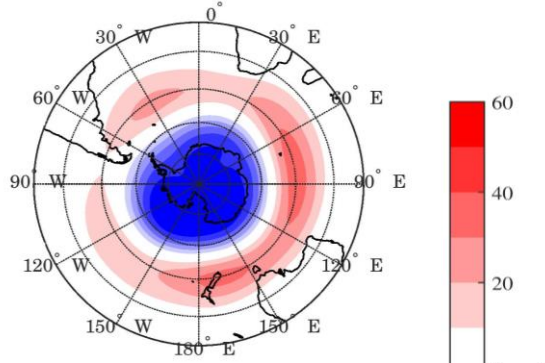
b) SAM EOF1 (21.0%) 20CRv2
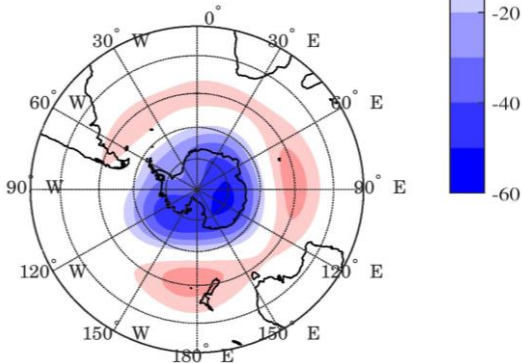
Figure 24 – The leading EOF modes of the monthly mean 500 hPa geopotential height field for the Southern Hemisphere (20º−90º S) for (a) BESM-OA2.5 and (b) for 20CRv2 Reanalysis. The results are shown as the 500 hPa geopotential height regressed onto the corresponding normalized PC time series (meters per standard deviation) over the period 1950−2005. The percentage of the variance explained by each EOF is indicated at the title of the figure. The contour interval is 10 m.
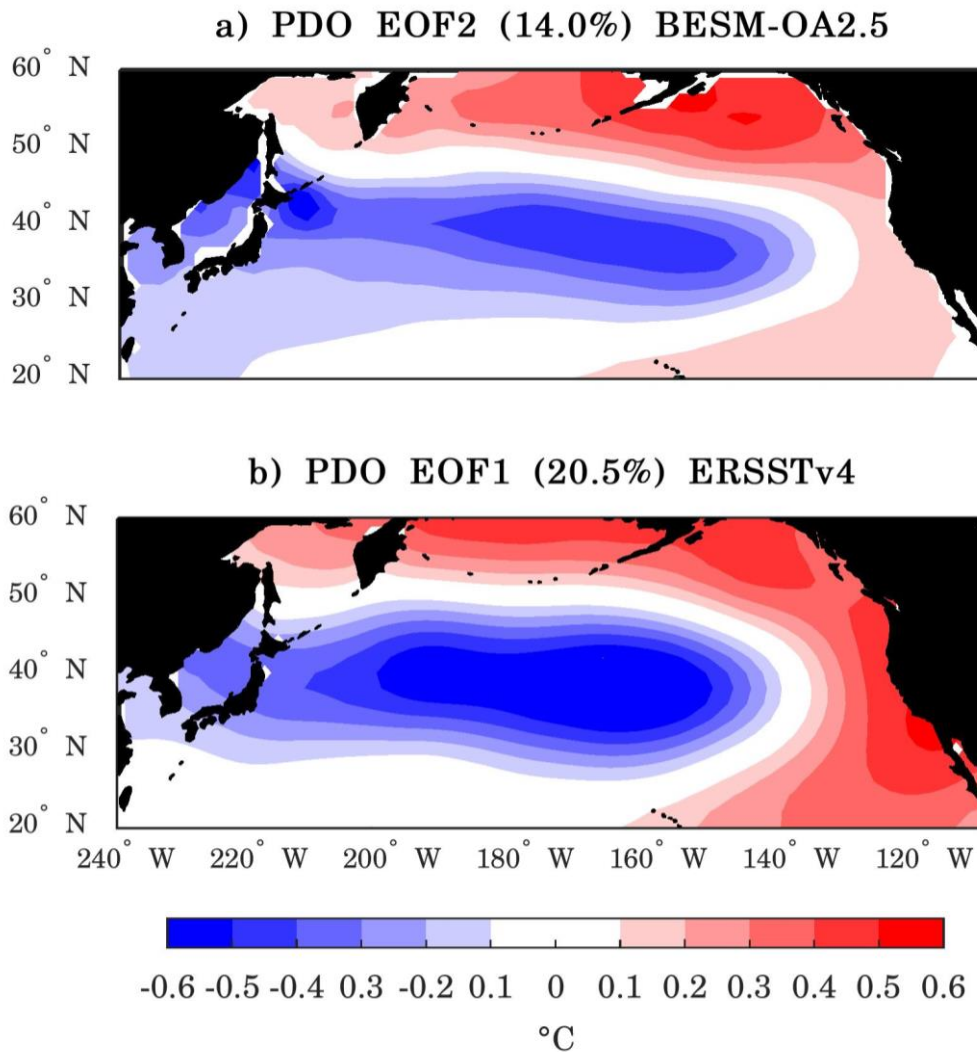
3   Figure 25 − (a) The second EOF mode of monthly SST anomalies of BESM-OA2.5 and

4   (b) the leading EOF mode of monthly SST anomalies of ERSSTv4, both over North

5   Pacific Ocean (20º−60º N; 240º−110º W). The results are shown as the monthly SST

6   anomalies regressed onto the corresponding normalized PC time series (℃ per standard

7   deviation) over the period 1900−2005. The percentage of the variance explained by

8   each EOF is indicated at the title of the figure. The contour interval is 0.1 ℃.
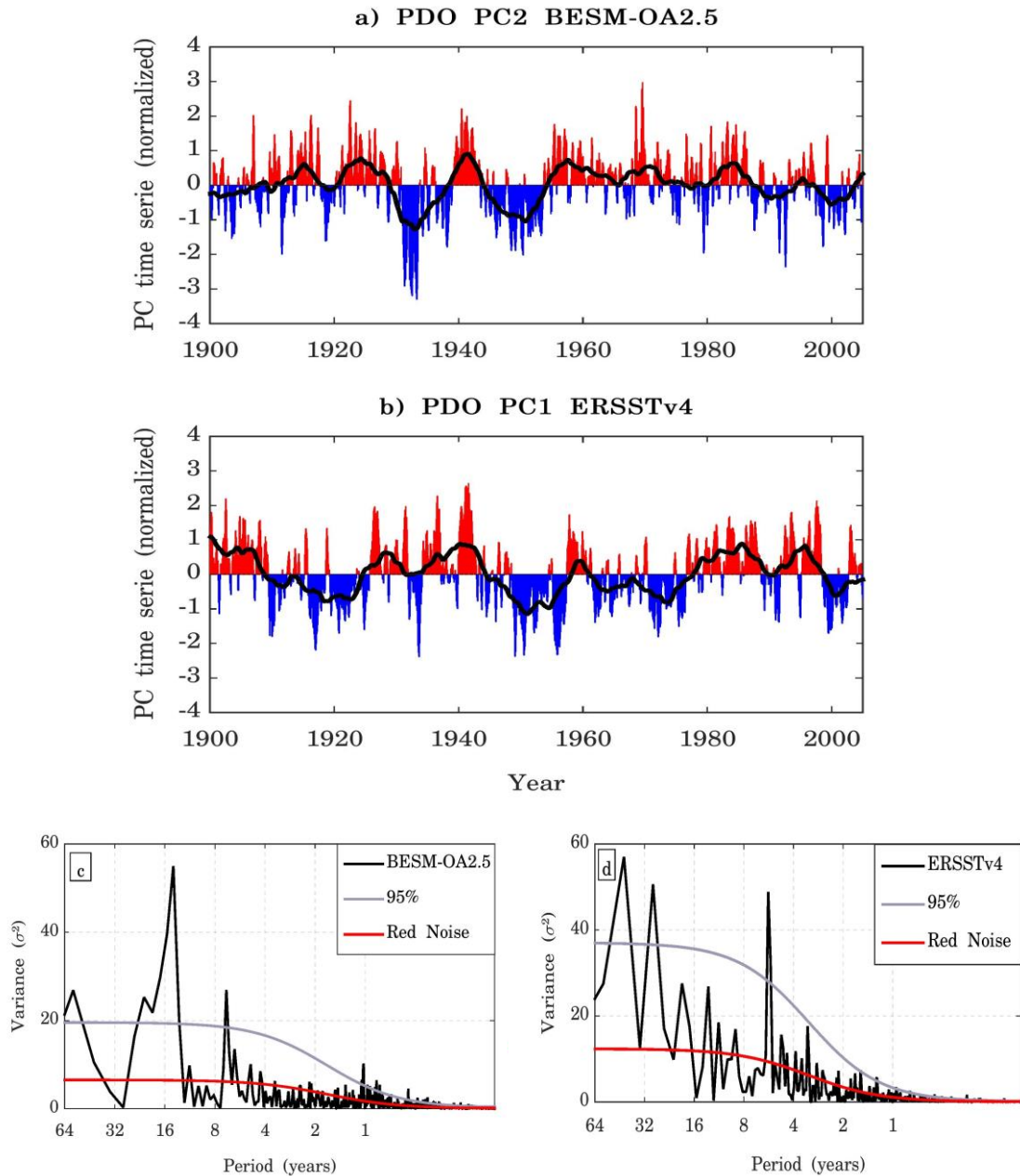
Figure 26 – Normalized second PC time series for (a) BESM-OA2.5 and normalized

leading PC time series for (b) ERSSTv4 over the period 1900–2005. The solid black

lines are the 5-year running average. Figures (c) and (d) are the power spectrum of the

second PC time series for BESM-OA2.5 and for the leading PC time series for 20CRv2,

respectively. The solid red line represents the theoretical red noise spectrum and the

gray line represents the 95 % confidence level.

Institute	Model	Simulation	horizontal resolution (lat×lon)	
			Atmosphere	Ocean
Commonwealth Scientific and Industrial Research Organisation/Bureau of Meteorology (Australia)	ACCESS1.3	Historical GHG r3i1p1	1.25 °×1.875 °	300×360 (tripolar)
Canadian Centre for Climate Modelling and Analysis (Canada)	CanESM2	Historical GHG r1i1p1	2.7906 °×2.8125 °	0.9303 °; 1.1407 °×1.40625
National Center for Atmospheric Research (USA)	CCSM4	Historical GHG r1i1p1	0.9424 °×1.25 °	384×320 (tripolar)
Centre National de Recherches Météorologiques/Centre Européen de Recherche et de Formation Avancée en Calcul Scientifique (France)	CNRM-CM5	Historical GHG r1i1p1	1.4008 °×1.40625 °	292×362 (tripolar)
Geophysical Fluid Dynamics Laboratory (USA)	GFDL-ESM2M	Historical GHG r3i1p1	2.0225 °×2.5 °	0.3344 °; 1 °×1 °
Goddard Institute for Space Studies (USA)	GISS-E2-H	Historical GHG r1i1p1	2 °×2.5 °	1 °×1 °
Met Office Hadley Centre (UK)	HadGEM2-ES	Historical GHG r1i1p1	1.25 °×1.875 °	0.3396 °; 1 °×1 °
L'Institut Pierre-Simon Laplace (France)	IPSL-CM5A-MR	Historical GHG r1i1p2	1.2676 °×2.5 °	149×182 (tripolar)
Japan Agency for Marine-Earth Science and Technology, Atmosphere and Ocean Research Institute (The University of Tokyo), and National Institute for Environmental Studies (Japan)	MIROC-ESM	Historical GHG r1i1p1	2.7906 °×2.8125 °	0.5582 °; 1.7111 °×1.40625 °
Meteorological Research Institute (Japan)	MRI-CGCM3	Historical GHG r1i1p1	1.12148 °×1.125 °	0.5 °; 0.5 °×1 °
Bjerknes Centre for Climate Research and Norwegian Meteorological Institute (Norway)	NorESM1-M	Historical GHG r1i1p1	1.8947 °×2.5 °	384×320 (tripolar)

2 Table 1 - List of models from CMIP5 with historical GHG simulations used to compare

3 with BESM-OA2.5. Models with higher resolution in the tropical region and a

1 decreasing resolution towards the poles have two values for latitude in their respective

2 oceanic resolution column. Models with oceanic tripolar grid, the number of grid points

3 in each coordinate are presented.